



# Continuous lifetime monitoring technique for structural components and main bearings in wind turbines based on measured strain and virtual load sensors

Bruno Rodrigues Faria <sup>1</sup>, Nikolay Dimitrov <sup>1</sup>, Nikhil Sudhakaran <sup>1</sup>, Matthias Stammler <sup>1,2</sup>, Athanasios Kolios <sup>1</sup>, W.Dheelibun Remigius<sup>3</sup>, Xiaodong Zhang<sup>4</sup>, and Asger Bech Abrahamsen <sup>1</sup>

Correspondence: Bruno Rodrigues Faria (brofa@dtu.dk)

#### Abstract.

Decisions on the lifetime extension of wind turbines require evaluating the remaining useful life of major load-carrying components by making a comparison to the design lifetime. This work focuses on the lifetime assessment of two fundamentally different components: a structural component in the form of the tower and rotating components in the form of the main bearings. A method is presented that combines high-frequency SCADA, accelerometers, minimally intrusive strain gauge at blade and tower, and limited design information for continued estimates of the component loads and their subsequent fatigue damage accumulations. The work is applied to a highly instrumented DTU research turbine, a Vestas V52 model, where strain gauges in the blade root and in the tower bottom are calibrated for nearly 10 years using continual calibration methods without the need for operator input. The lifetime estimates of the tower bottom and front and rear main bearings were found to be 1770 years and 166-333 years, respectively, reflecting the low average wind speed of the turbine site compared to the wind turbine design wind class IA. Secondly, it was investigated whether virtual load sensors can replace tower strain gauges and if one can use only uptower sensors for lifetime evaluation. Consistent tower bottom strain signal estimate and long-term damage accumulation were achieved with  $\pm 5\%$  lifetime variability once SCADA, nacelle accelerometers, and blade root strain gauges were combined for the deployment of a long short-term memory (LSTM) neural network. A systematic underprediction of the accumulated damage of the tower bottom was observed for the virtual load sensors, and a correction method was proposed. Finally, the impact of environmental conditions, including turbulence intensity and shear exponent of the incoming wind, on the main bearing lifetime was investigated using 10 years of measurements. A simple drivetrain thermal model was used to evaluate the modified lifetime  $L_{10m}$  of the main bearings, depending on the measured ambient temperature and the grease cleanliness assumptions. Higher fatigue loads are observed on the main bearings at rated wind speeds with low turbulence intensity and low shear. Changes of  $\pm 5$  °C in the ambient temperature around 15 °C caused a 10-year difference in the operational life of the main bearings at rated wind speed. It was also found that the specification of the gearbox mounting stiffness can lead to a 60% overprediction of the main bearing loads.

<sup>&</sup>lt;sup>1</sup>DTU Wind and Energy Systems, Technical University of Denmark, 4000 Roskilde, Denmark

<sup>&</sup>lt;sup>2</sup>Large Bearing Laboratory, Fraunhofer Institute for Wind Energy Systems IWES, 21029 Hamburg, Germany

<sup>&</sup>lt;sup>3</sup>Shell India Markets Private Limited, 562149 Bengaluru, India

<sup>&</sup>lt;sup>4</sup>Science and Technology Institute, China Three Gorges Corporation, 101100 Beijing, China

Preprint. Discussion started: 11 November 2025

© Author(s) 2025. CC BY 4.0 License.



35



#### 1 Introduction

The extension of the lifetime of wind turbines provides an opportunity to decrease the levelized cost of the electricity produced by wind turbines, which is not only competitive, but in many cases the cheapest electricity source according to evaluations of multiple global benchmark reports such as (IEA and NEA, 2020; IRENA, 2024). At the same time, lifetime extension could decrease the global warming potential ( $CO_{2,eq}$  / kWh) emitted during the entire life cycle of a wind turbine (UNECE, 2022).

Lifetime extension of wind turbines is then strongly dictated by reliable technical evaluations of the consumed and of the remaining useful lifetime of structural components such as the tower and the foundations as described by (Ziegler et al., 2018; IEC-TS-61400-28, 2020). Such large components are site-specific and little to no experience can be found in replacement of those during the lifetime and beyond, as this would hinder the profitability of a wind farm. Similarly, having unexpected and several load-carrying components failing would require long-lasting replacements that would increase the operational expenditure (OPEX) of a wind farm and reduce its revenue. That is the case with the main bearings. OPEX estimates should be based on the probability of failure of such components combined to their availability in the spare market.

As a failure in the main bearing means a failure in turbine operation, this decision should be made with high levels of certainty. A main bearing failure results in high replacement costs, between \$225,000 and \$400,000, loss of revenue due to production interruption, and its failure is one of the main reasons for the increase in OPEX, especially in onshore wind turbines of 2 to 6 MW in size according to Pulikollu et al. (2024). Although main bearings are known to have multiple failure modes, as examined by Hart et al. (2020), including abrasive and adhesive wear and fretting, this work considers lifetime consumption as the fatigue life consumption of the main bearing. This is due to the leading role of rolling contact fatigue (RCF) which can not yet be ruled out with respect to historical replacement data of the main bearings. Hart et al. (2023) carried a large review of historical data on the damage and failure of the main bearing and identified that for a large share (80%) of the reported failure, spalling was present, which could be a consequence of both subsurface- and surface-initiated RCF.

In this context, the end goal of a well-designed structural health monitoring (SHM) campaign is to have the most comprehensive and reliable wind turbine monitoring and lifetime estimation with the least amount of instrumentation Santos et al. (2022). And using strain gauges often results in one key drawback: compromised long-term reliability. There has been a literature gap on the possibility of calibrating strain gauges for many years, with some studies to mention Pacheco et al. (2024). So, the question of how to extrapolate the lifetime of components based on limited recordings has been of interest and widely investigated (Loraux and Brühwiler, 2016; Hübler and Rolfes, 2022; Sadeghi et al., 2024; de N Santos et al., 2024). However, no consensus has yet been reached on the methods or uncertainties related to those methods. In this context, data-driven methods Dimitrov and Göçmen (2022); Pimenta et al. (2024) deployed as long-term virtual load sensors could yield several advantages by replacing real sensors and reducing the amount of instrumentation needed, being able to describe complex mathematical correlations, with no real physical understanding of the system.

Considering the challenges and gaps identified, this work aims to maximize coverage using existing onboard sensors and limited non-invasive hardware additions, to evaluate the lifetime of structural and rotating component simultaneously. Based on this objective, the following research questions guided the methodology and subsequent analysis.

Preprint. Discussion started: 11 November 2025

© Author(s) 2025. CC BY 4.0 License.



60



- Is it possible to continuously and reliably count the lifetime of a tower and a four-point configuration main bearing without blade design information and having in hands SCADA, blade root, and tower bottom strain gauges, while meeting ISO-281 (2007) and IEC 61400-1 (2019) standards?
- What degree of accuracy could be achieved by a tower bottom virtual load sensor based on measurements in the nacelle?
- What are the environmental and operation conditions (EOC) which have strongest impact on the basic and modified rating lifetime of the main bearing ( $L_{10}$  and  $L_{10m}$ , respectively), based on analysis of a long-term measured dataset?

The remaining sections of this paper are organized as follows. Section 2 provides an overview of the theoretical background relevant to this work, including the assumptions behind the tower fatigue lifetime and the main bearing lifetime, as well as the concept of virtual load sensors applied in this study. Section 3 describes the wind turbine and the environmental measurement campaign used for data collection. Section 4 details the proposed methodology for the calibration of the strain gauge and the lifetime of the tower and main bearing based on load measurements and virtual load sensors. The results obtained are presented in Section 5, followed by a discussion in Section 6, where the findings are compared to the relevant literature and key correlations are analyzed. Section 7 concludes the paper by summarizing the main insights and learnings from this work.

# 70 2 Theoretical background

Behind the key assumptions of this work, mentioned in the introduction and shown in Figure 2, some require further explanation. The concept of tower fatigue and main bearing lifetime is assumed as derived in standards used for design and certification. The concept of virtual load sensors can also be very broad. In this work, we will focus on time-series and data-driven virtual load sensors that could be used to replace tower bottom strain gauges at a wind farm level and keep instrumentation in the nacelle. More details of each subject are described in the following subsections.

# 2.1 Tower fatigue lifetime

The lifetime is estimated as described by IEC 61400-1 (2019), considering the Design Load Cases (DLCs) 1.2 (Power production), 3.1 (Start-up) and 4.1 (Normal Shutdown). More details on how to classify these operational conditions based on 10-min SCADA can be found in Faria et al. (2024). On the material side, the DTU research tower V52 is made of structural steel S355, which is often used in large components and harsh environmental conditions. In this work, the fatigue assessment of critical welds assumes that the component has inherent defects in the welded joints and thus does not model crack initiation or growth. The first step is to convert a measured tower bending strain  $\epsilon$  [ $\mu$ mm/mm] to bending stress  $\sigma$  [Pa] as shown by Hooke's rule

The first step is to convert a measured tower bending strain  $\epsilon$  [ $\mu$ mm/mm] to bending stress  $\sigma$  [Pa] as shown by Hooke's rule  $\sigma = E \cdot \epsilon$ . The bending stress can be translated into the bending moment M assuming the tower is a Euler-Bernoulli beam.

$$\sigma = \frac{M \cdot c}{I} \tag{1}$$

where I [m<sup>4</sup>] is the area moment of inertia and c [m] is the radius, in the case of a circular cross section. To evaluate fatigue, the stress time series is converted to stress ranges  $\Delta \sigma_i$  and umber of cycles  $n_i$  using the rainflow counting technique, as described





by ASTM E1049-85 (2017). The tower bottom in this work is evaluated using the category of the stress cycle (SN) curve category "D", for butt-weld in air as suggested by DNVGL-RP-C203 (2016), which translates  $\Delta \sigma_i$  into a maximum amount of cycle to failure  $N_{max,i}$ . Finally, fatigue accumulation, in other words, fatigue lifetime is assumed to be linear, according to Palmgren and Miner (1945), which is valid for any time window, from high-frequency to 10-min instances to lifetime.

$$D_T = \sum_{j}^{N_j} D_{T,j} = \sum_{i}^{N_j} \sum_{i}^{N_i} \frac{n_i}{N_{max,i}} = \sum_{j}^{N_j} \sum_{i}^{N_i} \frac{n_i \cdot (\Delta \sigma_i)^{m_i}}{K_i}$$
 (2)

where  $D_T$  is the tower accumulated fatigue damage (failure at unity),  $D_{T,j}$  is the accumulated fatigue damage of the 10-minute instance,  $m_i$  is the exponent of the SN curve,  $K_i$  is the intercept of the SN curve on the y-axis,  $N_j$  is the number of 10 min instances and  $N_i$  is the number of cycles in a given instance.

The exponential nature of fatigue can be observed and its non-linearity due to different  $m_i$  and  $K_i$  dependent on the two regions of the SN curve where the cycle could be placed. In order to facilitate the evaluation of virtual load sensor during training and validation, instead of comparing  $D_T$ , Damage Equivalent Loads (DELs) are often used and can be explained as single-frequency sinusoidal loads that would inflict the same damage as the initial load variable in time, as in

$$DEL = \left(\sum_{i}^{N_i} \frac{n_i \cdot \Delta \sigma_i^m}{N_{ref}}\right)^{1/m} \tag{3}$$

where m is assumed to be 4, which is an average between DNV "D" curve values of  $m_i$  equal to 3 and 5 and  $log_{K_i}$  equal to 12.164 and 15.606, respectively, transitioning at  $N_{max}$  equal to  $10^7$  cycles. The  $N_{ref}$  is a normalization factor and is arbitrarily assumed to be  $10^7$  cycles, since DEL has no absolute reasoning.

However, for the estimation of the consumed and remaining useful lifetime of a tower, and the deployment of the virtual load sensor in the long-period, DEL has no absolute meaning and its uncertainty underestimates the uncertainty of the useful life of the component and, therefore,  $D_T$  should be prioritized. More discussion is present in Section 5.3.

#### 2.2 Main bearing fatigue lifetime

110

The lifetime of a rotating component, such as a main bearing, can be significantly more complex to model than the tower lifetime. In this work, the formulations from ISO-281 (2007) are followed, which also defines the linear accumulation of damage as proposed by Palmgren, using the same DLCs as for the tower. As mentioned, rolling contact fatigue is not the only damage mode of the main bearings, but the inclusion of additional mechanisms is not in the scope of the present work.

The radial  $F_r$  [N] and axial  $F_a$  [N] load acting on the main bearings are combined into

$$P = X \cdot F_r + Y \cdot F_a[N] \tag{4}$$

where P is the dynamic load, X and Y are functions of the load ratio  $F_a/F_r$  and the limiting value e. The time-varying P can be replaced by a constant load  $P_{eq}$  that would have the same deterioration at its given operational rotation speed, similar to the defined DEL, without involving any counting method.

$$P_{eq} = \left(\frac{\sum P_i^p \cdot \omega_i}{\sum \omega_i}\right)^{1/p} \tag{5}$$



135

140



where  $P_i$  [N] is the dynamic load and  $\omega_i$  [rpm] is the rotational speed of the main bearing at the instantaneous i timestamp.

Then, the basic rating life  $L_{10}$  is defined as the 90% survival time of a given population of main bearings under similar operational conditions. In other words, 10% of the bearings would fail.

120 
$$L_{10,j} = 10^6 \left(\frac{C_d}{P_{eq}}\right)^p \text{[revolutions]} \qquad L_{10,j} = \frac{10^6}{60 \cdot \omega \cdot 8760} \left(\frac{C_d}{P_{eq}}\right)^p \text{[years]} \qquad L_{10} = \frac{1}{\sum \phi_j / L_{10,j}} \text{[years]}$$
 (6)

where  $L_{10}$  is the basic rating life overall while  $L_{10,j}$  is the basic rating in a given 10-minute instance j. If all instances have the same 10-min,  $\phi_j$  is the inverse of the number of instances.  $C_d$  [N] is the dynamic load rating, p is the exponent function of the rolling body type (e.g. ball or roller) as provided by ISO-281 (2007),  $P_{eq}$  [N] is the dynamic equivalent load and  $\omega$  [rpm] is the rotational speed of the main bearing within a 10-min instance. Once  $L_{10}$  is calculated as the number of hours to failure in each instance, one can describe a main bearing damage accumulation, similar to the damage accumulation in the tower, as in

$$D_B = \sum_{j}^{N_j} D_{B,j} = \frac{t_{operation}}{L_{10}} \tag{7}$$

where  $D_B$  is the accumulated fatigue damage of the main bearing (failure at unity),  $D_{B,j}$  is the accumulated fatigue damage of the 10-minute instance, and  $t_{operation}$  is the evaluated time of operation in years.

In order to incorporate a more realistic effect of operating conditions on the main bearing, a life modification factor  $a_{\rm ISO}$  should be evaluated. The latter considers that the lubricant will be exposed to different operating temperatures and its value will be affected by the level of grease cleanliness, the operating viscosity (function of temperature), the rolling element type, bearing fatigue limit, and external loads. The complete formulation can be found in ISO-281 (2007). The modified rating life  $L_{10m}$  of a main bearing is then calculated using

$$L_{10m} = L_{10} \cdot a_{\rm ISO} \tag{8}$$

#### 2.3 Virtual load sensors

In this work, virtual load sensors are seen as an opportunity to replace physical sensors to estimate tower bottom bending moments and long-term fatigue lifetime, keeping the necessary measuring in the nacelle. In the literature, several efforts have been made in the regard of data-driven (machine learning) models for lifetime predictions of components.

Benefiting from instances statistics and more available SCADA accelerometers, efforts were made to estimate target statistics such as damage equivalent loads (DELs) or damage to the main bearing. Mehlan et al. (2023) estimates aerodynamic hub loads and tracked bearing fatigue damage using a digital-twin based virtual sensing combining SCADA and condition monitoring. For support structures, de N Santos et al. (2024) estimates the fatigue lifetime based on different combinations of SCADA levels, highlighting the improvement in performance using reliable nacelle accelerometers, with a novel population-based approach for wind farm extrapolation. Focusing on time extrapolation, Hübler and Rolfes (2022) focuses on different methodologies to extrapolate damage in time and their estimated uncertainty. On the other hand, when the time series signal is the target output, the model selection and training process are quite different. Complementary, Dimitrov and Göçmen (2022) shows how machine learning time series models (e.g. LSTM) can act as virtual sensors for blade root bending moment trained

Preprint. Discussion started: 11 November 2025

© Author(s) 2025. CC BY 4.0 License.



150

155

160

165

170

175

180



on aeroelastic simulations. More recent efforts extend virtual sensing to floating turbines. Gräfe et al. (2024) trained neural networks on simulated floater motions and LIDAR-derived wind to reconstruct fairlead tensions and DELs.

The same data-driven models applied by Dimitrov and Göçmen (2022) are selected to be used in this work on the DTU research V52 turbine dataset, all derivatives of neural network architectures. This work contribution to virtual load sensor methods lies in the validation of a model that should accurately replicate both: (1) the time series of tower bottom bending moments and (2) the fatigue loads of the tower and main bearings in the long term. (1) The first can have its performance quantified by feeding the virtual load sensor as a thrust estimate to calculate the lifetime consumption of the main bearings. (2) The latter includes the 3 most damaging operational conditions for the tower as described in Pacheco et al. (2024); Faria et al. (2024): power production DLC 1.2, start-up DLC 3.1, and shutdown DLC 4.1, all in a single model.

#### 3 Measurements

In this work, SCADA data and measurements from nearly 10 years are analyzed from February 2016 to December 2024 at Risø, Denmark. The environmental conditions are analyzed out of 10-min instances statistics from a met mast about 100 m east of the DTU research V52 turbine. In addition to the mean wind speed  $U_{hub}$  at the hub height of  $z_{hub} = 44$  m, the turbulence intensity is calculated as  $TI = \sigma_U/U$ , where  $\sigma_U$  is the standard deviation of the wind speed. Moreover, vertical shear is modeled considering the normal wind profile model IEC 61400-1 (2019) given by the power law equation  $U(z) = U_{hub}(z/z_{hub})^{\alpha}$ , where z is the height and  $\alpha$  is the shear exponent. The latter is estimated as the best fitting factor out of five different cup anemometers measuring heights (at 18, 31, 44, 57 and 70 m) for each 10-min instance. No shadow correction was performed for the mast tower. In general, it is possible to observe that the Risø site has fairly low wind and constant conditions. The yearly wind speed  $U_{hub}$ , estimated as a Weibull function in the graph on the left, has a mean below 6 m/s. The site reference turbulence  $I_{ref}$  calculated as  $I_{ref} = \sigma_U/(0.75U_{hub} + 5.6)$ , has a mean value around 0.08 (closer to IEC class C) and the shear exponent  $\alpha$  of 0.22. The prevailing wind direction falls within the southwest quadrant across all years. The DTU research V52 turbine is a Vestas 850 kW onshore wind turbine class IA with a rotor diameter of 52 m and a hub height of 44 m, with a active pitch and rotor speed control. SCADA and SHM measurements are available from February 2016 to December 2024, as are statistics and high-frequency data. The turbine has a rated wind speed of approximately 14 m/s. Figure 1 represents the turbine schematic and part of its instrumentation, highlighting the two measurement setups present in the tower bottom (a–a) and blade root (b–b). SCADA includes rotor speed  $\omega$ , pitch angle  $\theta$ , yaw angle  $\gamma$ , azimuth angle  $\varphi$ , and power. All of the bending moments shown are obtained from full Wheatstone bridge installed in the components. This configuration has a couple of important advantages as higher signal-to-noise ratio, is temperature independent and optimized for measuring bending stress, see Hoffmann (1989). A problem in the quality of the measured azimuth angle  $\gamma$ , carried out by a proximity sensor on the shaft flange, was identified before 2018 and after 2022, probably due to surface dirt. A correction was applied to all the raw signal to account for that, by combining the controller rotor speed signal with the measured azimuth to have a more reliable estimate of the azimuth angle (please refer to Appendix A). Taking into account Figure  $1(c_1)$ , the tower bottom fore-aft bending moment  $M_{fore-aft}$ (downwind) can be calculated as in Equation 9.





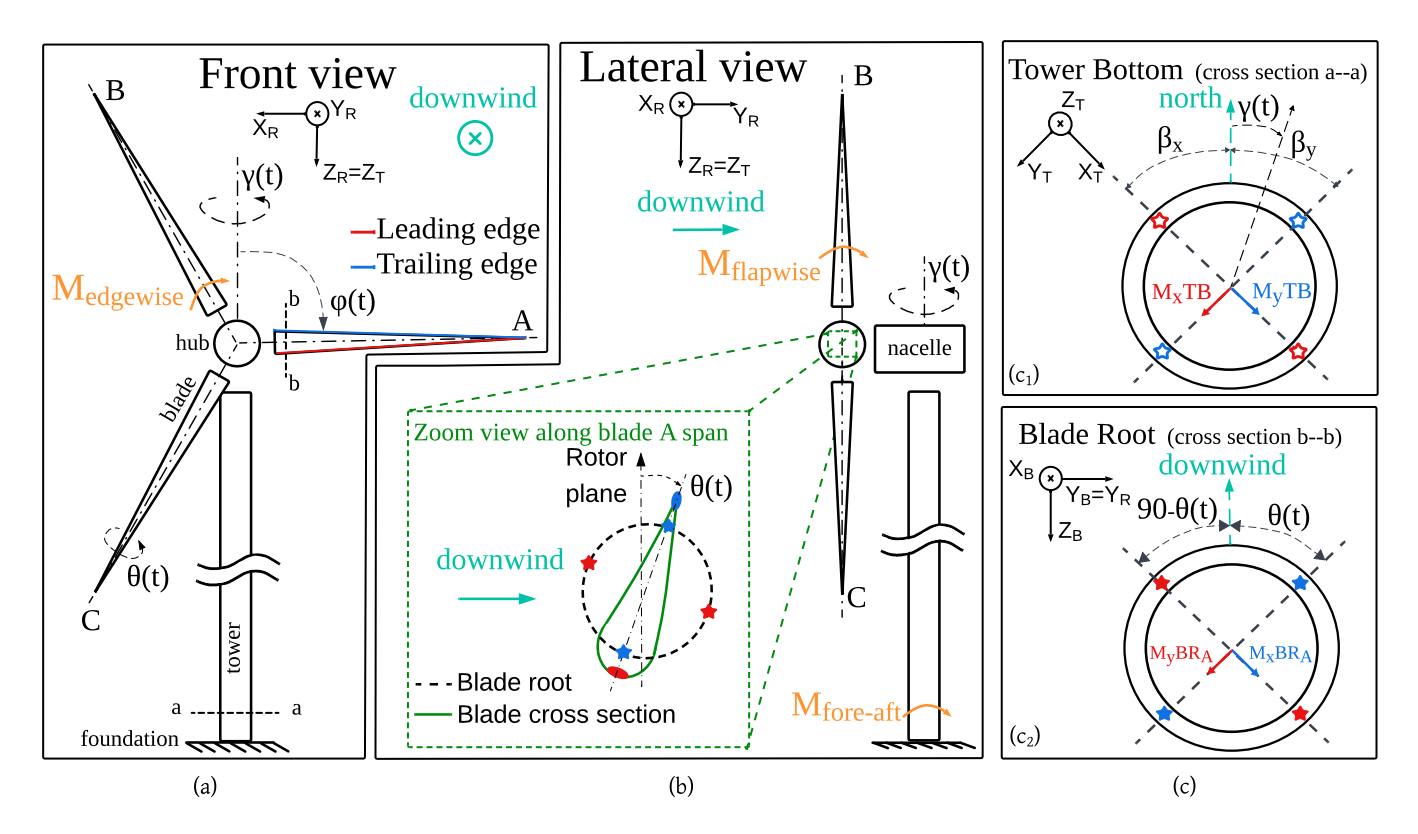


Figure 1. Schematic of an onshore wind turbine to represent the DTU research V52 turbine parameters and measurements. (a) Front view shows the rotor coordinate system XYZ<sub>R</sub> which moves with the yaw angle  $\gamma(t)$  around Z<sub>T</sub> and is facing the wind direction. The azimuth angle  $\varphi(t)$  of blade A and pitch angle  $\theta(t)$  are also shown. The  $M_{edgewise}$  represents the edgewise (in-plane) blade root bending moment. (b) In the lateral view, the flapwise (out-of-plane) rotor bending moment  $M_{flapwise}$  and the tower bottom fore-aft bending moment  $M_{fore-aft}$  are shown. The  $\theta(t)$  angle is the controller-defined blade root angle between the rotor plane and the chord line of the blade, as shown in the zoom view (green dashed box). (c<sub>1</sub>) Tower bottom cross section (a–a) in the global/tower coordinate system (time-invariant) XYZ<sub>T</sub> is determined.  $M_{fore-aft}$  is dependent on  $\gamma(t)$ , as a composition of the measured tower bottom bending moments MxTB and MyTB, which are installed at the angles  $-\beta_x$  and  $\beta_y$  respectively. (c<sub>2</sub>) Blade root A cross section (same setup for blades B and C) shown in the blade coordinate system XYZ<sub>B</sub>, which rotates with  $\varphi(t)$  in respect to Y<sub>R</sub>. Both measured blade root bending moments  $M_xBR_A$  and  $M_yBR_A$  shall be converted into  $M_{flapwise}$  and  $M_{edgewise}$  as function of the pitch angle  $\theta(t)$ .

$$M_{fore-aft}(t) = \frac{(-M_x TB(t) \cdot \sin(\beta_y - \gamma(t)) + M_y TB(t) \cdot \sin(\beta_x + \gamma(t)))}{\sin(\beta_x + \beta_y)}$$
(9)

in which the denominator factor is imposed because the two tower bottom bending moments are not perpendicular. Similarly, considering the measurement setup shown in Figure  $1(c_2)$ , the blade root flapwise  $M_{flapwise}$  (out-of-plane) and edgewise





 $M_{edgewise}$  (in-plane) bending moments can be calculated individually for blades A,B and C.

$$5 \quad M_{flapwise,(A,B,C)}(t) = M_x B R_{(A,B,C)}(t) \cdot \cos(\theta(t)) - M_y B R_{(A,B,C)}(t) \cdot \sin(\theta(t))$$

$$\tag{10}$$

$$M_{edgewise,(A,B,C)}(t) = M_x B R_{(A,B,C)}(t) \cdot \sin(\theta(t)) + M_y B R_{(A,B,C)}(t) \cdot \cos(\theta(t))$$

$$\tag{11}$$

#### 4 Methodology

190

Figure 2 shows the inputs and assumptions taken into account to investigate the research questions. From high-frequency turbine measurements to tower (structural component)  $D_T$  and main bearings (rotating component)  $D_B$  accumulation of fatigue damage over time. The orange boxes include the continual calibration of the strain gauges and the operations to translate the strain measurements of the tower and the blade to the tower bottom bending moment  $M_{fore-aft}$ , and the axial  $F_a$  and radial  $F_r$  main bearing loads. The standards shown (DNVGL-RP-C203, 2016; IEC 61400-1, 2019; ISO-281, 2007) provide the methods for the fatigue lifetime evaluations of each component, as explained in Section 2. The DTU research V52 turbine is assumed to have a S355 steel tower, with a measured tower geometry consisted of an 2.913 m outer diameter and 16 mm wall thickness.

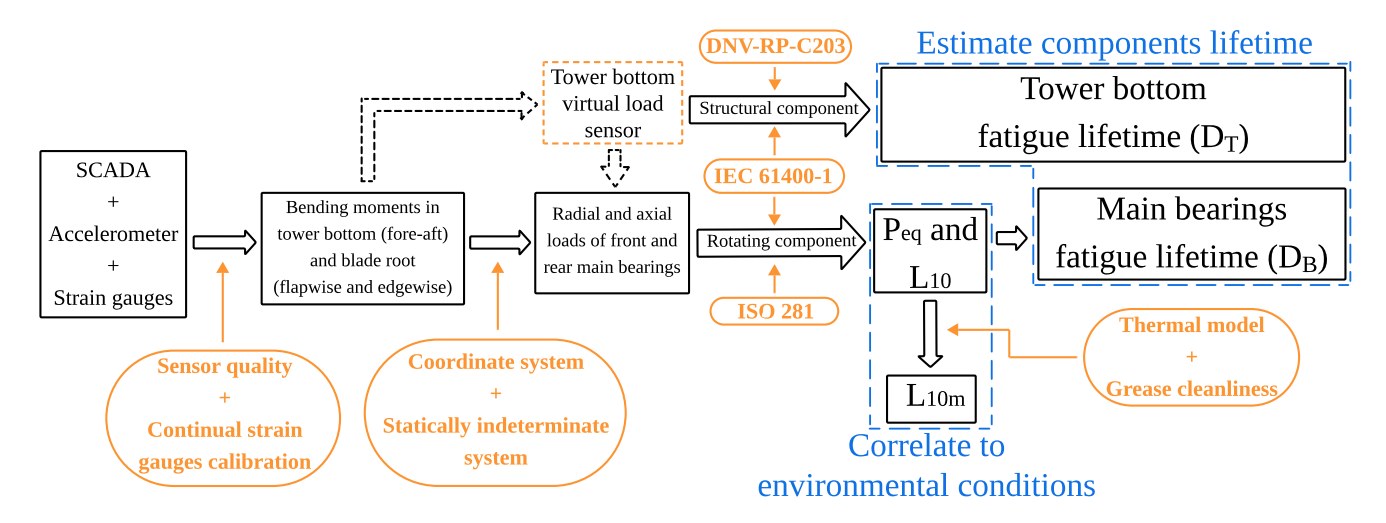


Figure 2. Methodology flowchart presenting the steps followed in this work, starting from high frequency measurement and SCADA dataset, to components lifetime estimates. Rectangular black boxes refers to measurement signals and estimates. Tower bottom  $D_T$  and main bearings  $D_B$  fatigue lifetime are analyzed over time, and the equivalent dynamic load  $P_{eq}$ , basic rating life  $L_{10}$  and modified rating life of the main bearing  $L_{10m}$  are analyzed as function of environmental conditions. Orange boxes identify the procedures and standards used in this work. The orange dashed box contains the tower bottom virtual load sensor, which should replace the real sensor in case of sensor failure.

In addition, a virtual load sensor is proposed to replace real strain gauges in the event of sensor failure and its performance is assessed for fatigue lifetime estimations. While, the main bearings equivalent dynamic load  $P_{eq}$ , the basic  $L_{10}$  and modified  $L_{10,m}$  rating life are evaluate as function of key environmental conditions. To compute the  $L_{10,m}$  of the main bearings, a

Preprint. Discussion started: 11 November 2025

© Author(s) 2025. CC BY 4.0 License.



200

205

215

220

225



drivetrain thermal model was made to estimate the temperature of the main bearings, which is necessary to estimate the life modification factor  $a_{\rm ISO}$ , as introduced in Section 2.2.

#### 4.1 Strain gauge zero-drift automatic calibration

It is often claimed that strain gauges are only reliable for short-term (less than a year) to mid-term (couple of years) campaigns, a limitation that would conflict with the requirement for sustained monitoring of wind turbine structural elements, most notably in offshore installations, where replacement in case of sensor failure is expensive and can take time due to weather windows.

This work overcomes such limitation by introducing continual and automated routines for the calibration of both tower bottom and blade root strain gauges that work on long-term datasets (almost a decade). The methods do not require operator intervention, stopping or curtailment, and instead take advantage of idling and parked conditions. Both methodologies are derived from the recommendations in IEC 61400-13 (2016). The main objective is to identify the artificial offset O from the measured strain gauges and to correct them to the original zero point. No external dynamic load should cause zero strain. The signals of the bending moment shown in Figure 1 should be understood as  $M = G \cdot (M_{raw} + O)$ , where M is the corrected bending moment,  $M_{raw}$  is the measured strain signal, G is the gain associated with the translation of voltage readings into bending moment, and O is the artificial offset of the strain sensor. It should be noted that for the tower bottom strain gauges placed on steel, G can be analytically calculated, depending on the bridge arrangement (full bridge Wheatstone in the DTU research V52 turbine), the elastic modulus and the geometry. However, for blade root strain gauges mounted on composite material, a blade pull exercise must be performed to estimate G. And a crosstalk correction has to be applied considering the geometry of the twisted and nonsymmetric blade, see Papadopoulos et al. (2000). Such calibration campaign has been undertaken on the DTU research V52 turbine, but the detailed results are not presented in this work for confidentiality reasons.

#### 4.1.1 Yaw sweeps and Low-Speed Idling (LSI)

The tower bottom strain gauges calibration is based on a specific operation in which the wind turbine is parked and untwists its power cable at low wind speed. In that case, the turbine performs full yaw rotations and the main contribution to the tower bottom bending moment is the gravitational load from the nacelle mass hanging bending moment. In case at least 1-minute data points of the yaw angle  $\gamma$  are available, the high-frequency strain gauge signals  $M_xTB$  and  $M_yTB$  can be automatically calibrated Faria et al. (2024). The Python package generated for this matter is publicly available at Faria and Jafaripour (2023). The blade root strain gauge calibration is performed based on both idling and parked conditions at low wind speed. The first is used to calibrate the strain gauges placed on the pressure-suction surfaces of the blade. The latter is for those on the leading-trailing edges. The azimuth angle  $\varphi$  is needed at a higher sampling frequency (e.g. tested with at least 1 Hz). More information on the implementation can be found in Pacheco et al. (2024) and Faria et al. (2025).



235



# 4.2 From blade and tower to main bearing loads

The front and rear main bearings of the DTU research V52 turbine are described in Table 1. The drivetrain transmits the torque from the rotor to the gearbox through the main shaft, which is supported by two spherical roller bearings in the main bearing housing and the gearbox upfront bearing as shown in Figure 3a.

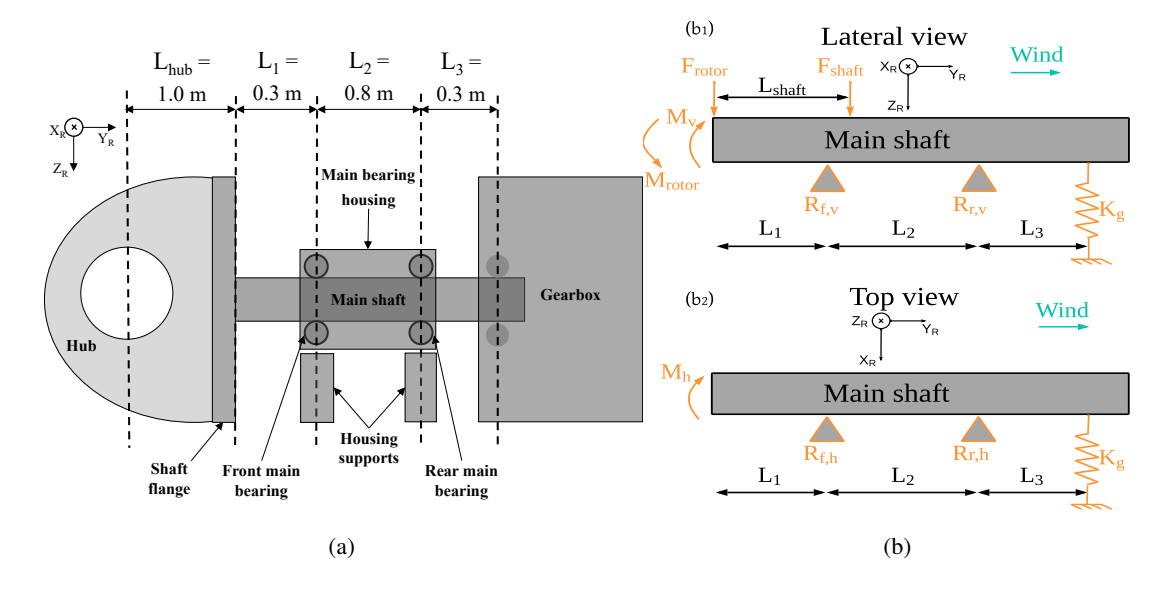


Figure 3. (a) Schematic of the DTU research V52 drivetrain. The hub carries the blades and is bolted to the shaft flange. The shaft is supported by two main bearings, which are mounted inside the main bearing housing. The latter is clamped to the nacelle bedplate through the housing supports, similarly the gearbox is mounted by the torque-arms but in two non-rigidly stiff connection points. (b1) refers to the lateral view used to derive the vertical radial loads in the main bearing and (b2) refers to the top view used to derive the horizontal radial loads. The  $M_v$  and  $M_h$  are the vertical and horizontal aerodynamic resultant bending moments from the rotor, while  $F_{rotor}$  and  $F_{shaft}$  are the rotor and shaft gravitational loads due to their weight and  $M_{rotor}$  is the bending moment associated with the shift of  $F_{rotor}$  from the hub center to the shaft flange by  $F_{hub}$ . As for the reactions, radial loads are given by  $F_{hub}$ , classified as  $F_{hub}$  for front,  $F_{hub}$  for vertical and  $F_{hub}$  for horizontal. The gearbox mounting stiffness is equally estimated in both direction and represented by the spring  $F_{hub}$ .

The main bearing housing is clamped to the nacelle bed plate, while the gearbox is mounted through its torque-arms in a rubber support. The rubber support is assumed to have a linear and temperature-independent spring with a stiffness of  $20 \cdot 10^6$  [N/m], close to the suggested values in Haastrup et al. (2011); Keller et al. (2016). A sensitivity analysis is performed later to evaluate the importance of this assumption. The static gravitational loads acting on the main shaft, shown in Figure 3b, are derived from a combination of public sources and visual inspections of the turbine nacelle. Similar for the lengths (e.g.  $L_{shaft}$ ). The gravitational force of the rotor  $F_{rotor}$  is calculated assuming a rotor and a hub mass of 10 tons (third party source, see Scribd (2021)). The gravitational force of the shaft  $F_{shaft}$  assumes a shaft mass equal to 1 ton, between an internal estimate of 0.8 tons and the Fingersh et al. (2006) estimate of 1.2 tons, which uses the best-fit equation  $m_{shaft} = 0.0142 \cdot D^{2.888}$  from historical data (given D as the rotor diameter in meters and the mass in tons).

© Author(s) 2025. CC BY 4.0 License.





**Table 1.** Technical specification of the two main bearings in the DTU research V52 turbine given by SKF Group (2025). SRB stands for spherical roller bearing and the bearing p is equal to 10/3.

	Designation	Туре	Inner diameter	Outer diameter	Basic dynamic load rating $C_d$	Basic static load rating $C_o$	Fatigue load limit $C_u$	limiting factor $e$
Front main bearing	23064	SRB	320 [mm]	480 [mm]	2348 [kN]	3800 [kN]	285 [kN]	0.23
Rear main bearing	23160	SRB	300 [mm]	500 [mm]	3368 [kN]	5100 [kN]	380 [kN]	0.3

Once static loads are defined, the aerodynamic bending moment driven by the blades in the vertical  $M_v$  and horizontal  $M_h$  directions can be estimated from the blade out-of-plane bending moments, using:

$$M_v(t) = M_{flapwise,A}(t) \cdot \cos(\varphi(t)) + M_{flapwise,C}(t) \cdot \cos(\varphi(t) + 120) + M_{flapwise,B}(t) \cdot \cos(\varphi(t) + 240)$$
(12)

$$M_h(t) = M_{flapwise,A}(t) \cdot \sin(\varphi(t)) + M_{flapwise,C}(t) \cdot \sin(\varphi(t) + 120) + M_{flapwise,B}(t) \cdot \sin(\varphi(t) + 240)$$
(13)

where  $\varphi(t)$  is the azimuth angle of blade A, see Figure 1. It should be noted that a positive  $M_v$  should benefit the loads in the radial main bearings to some extent, as it counter-balances  $F_{rotor}$ .

The main shaft is supported in 3 points, two main bearings and the gearbox, in both directions (lateral view and top view), so it is a statically indeterminate system. To solve it, the shaft is modeled as a flexible beam and a double integration method is applied to compute the radial load  $R_{f,v}$ ,  $R_{f,h}$ ,  $R_{r,v}$  and  $R_{r,h}$  (see Appendix B). The resultant radial loads of the front  $R_f$  and rear  $R_r$  main bearings have a magnitude of

250 
$$R_{(f,r)} = \sqrt{R_{(f,r),v}^2 + R_{(f,r),h}^2}$$
 (14)

, which are solved individually for each main bearing.

The axial load of the main bearings is equal to the thrust estimate, derived as the bending moment  $M_{fore-aft}$  divided by the height difference between the hub height and the tower bottom strain gauge. This is an assumption of this methodology, where the thrust estimate is linearly related to the bending moment of the bottom of the tower. Apart from that, since both bearings are able to carry axial load, the system could become over-constrained. An additional axial load would be applied to the bearings in the case of thermal expansion. For these reasons, the rear bearing is considered the locating bearing, being the larger bearing between the two.

# 4.3 Tower bottom virtual load sensor: thrust and fatigue loads

The selection of good candidates for the machine learning model to be deployed as virtual load sensors was carried out from simpler to more complex neural network architectures. Pure spatial correlation between the target variable and inputs is tested



280



using a feedforward neural network (FNN) baseline model (Rumelhart et al., 1986). Temporal correlation is added through an FNN with n-lagged time steps,NlaggedFNN Dimitrov and Göçmen (2022), and a Long Short-Term Memory (LSTM) neural network (Bengio et al., 1994). The first can only take a few time steps to still be "trainable", while LSTM is often a less noise sensitive model and can better capture long-term dependencies according to Bengio et al. (1994), at the cost of model complexity. The hyperparameters of the models were tuned using the Keras-tuner random search method O'Malley et al. (2019) using 5 h of data. The bounds and the optimal hyperparameters for the models that combine all possible inputs are included in Appendix C. All models used the "relu" activation curve in the hidden layers and "linear" activation towards the output layer. The LSTM model had a fixed "LSTM" layer and a second hidden layer with the same amount of neurons (hidden units) as the first layer. The size of the training data set was 160 h of data selected using a k-means clustering technique Pedregosa et al. (2011), spreading the training space within the rotor speed, blade pitch, power, and design load cases (DLC) to cover the relevant operational conditions. Similarly to Dimitrov and Göçmen (2022), a training dataset size and sampling frequency sensitivity were carried out to use optimum values. In addition to that, different input signals are tested. Starting from most available "SCADA" alone, including blade pitch, rotor speed, power, and azimuth (which was converted into sine and cosine), then either adding tower top "Accelerometer", or the flapwise bending moment from one or all blades (stated as "Strain"). And finally combining all available inputs as "All".

Figure 4 shows the power spectrum density (PSD) of the different normalized input signals. One hundred representative instances around the rated wind speed and similar turbulence and shear were analyzed. The different dynamic components with which the neural networks will be trained is visualized. It can be seen that all SCADA signals a high quasi-static component, while the azimuth has pronounced spikes around 1P, 3P, and 6P.

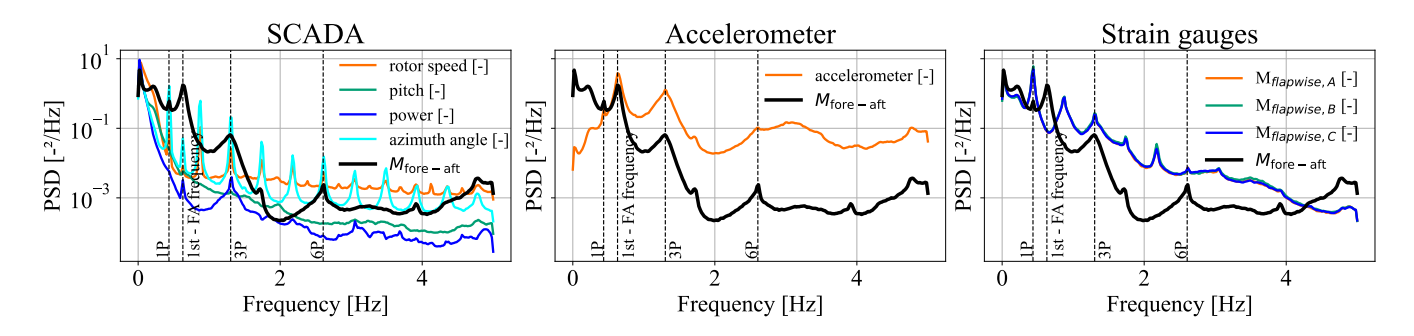


Figure 4. Normalized Power Spectrum Density (PSD) of the possible input signals to be used in the training of a time-series virtual load sensor. The black line is the target variable  $M_{fore-aft}$ . Normalization is based on the mean and standard deviation of each 10-min instance and signal. The spectrum is generated by averaging 100 instances at rated wind speed (14 m/s) to generate a smooth PSD chart.

However, only the accelerometer signal can well capture the first fore-aft turbine frequency (around 0.62 Hz Rinker et al. (2018)), while its amplification of higher frequency components compared to  $M_{fore-aft}$  cannot be considered pure electrical noise. When testing in standstill/parked conditions, there is strong attenuation similar to the  $M_{fore-aft}$  PSD. The most consis-





tent explanation is that the gearbox operation feeds high-frequency broadband vibrations through the bedplate into the nacelle accelerometer, elevating the spectrum beyond a discrete peak.

The performance metrics selected are the Normalized Root Mean Square Error (NRMSE), which is normalized by the standard deviation  $\sigma_y$  instead of the mean signal to avoid overshoot in case of small mean values. To validate fatigue lifetime estimates, the equivalent damage load DEL and  $P_{eq}$  are analyzed in terms of the mean absolute error (MAE).

$$NRMSE = \frac{1}{\sigma_y} \sqrt{\frac{\sum_{i=1}^{N} (Y_{\text{pred},i} - Y_{\text{meas},i})^2}{N}}$$
(15)

$$MAE_{Load=(DEL, P_{eq})} = \frac{1}{N} \sum_{i=1}^{N} \left| \frac{Load_{pred, i} - Load_{meas, i}}{Load_{meas, i}} \right| \times 100$$
(16)

where  $Y_{pred}$  is the time instant prediction,  $Y_{meas}$  is the measured of  $M_{fore-aft}$ , and N is the number of instances included.

#### 4.4 Drivetrain thermal model

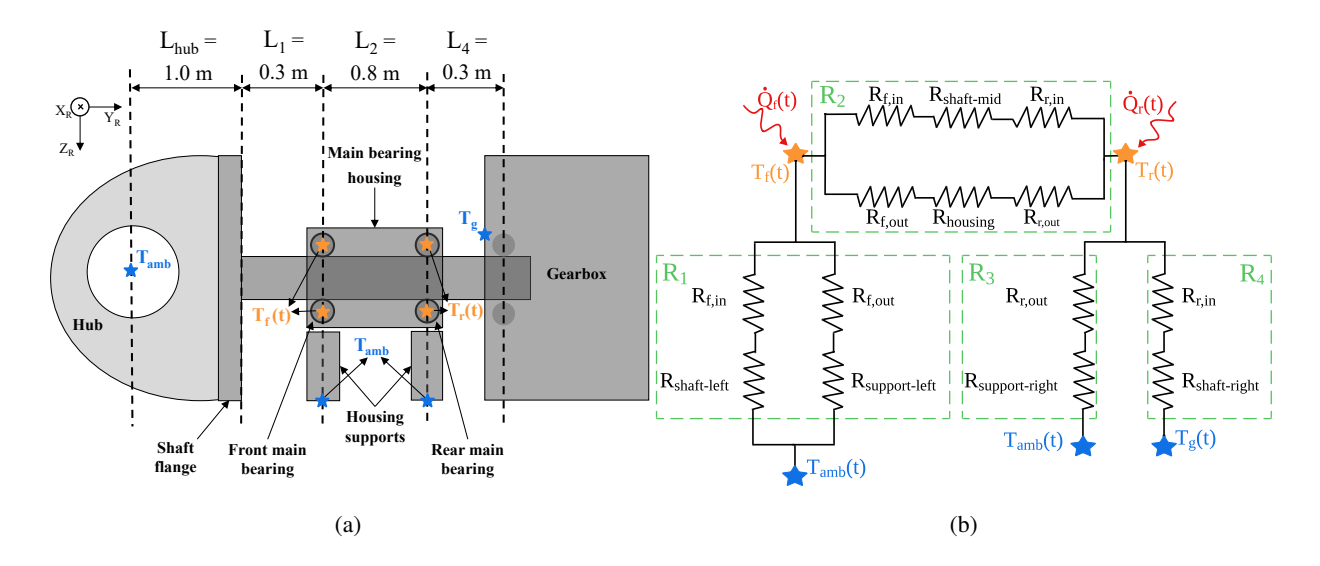


Figure 5. (a) Schematic of DTU research V52 turbine drivetrain with the main bearing estimated front and rear temperature  $T_f$  and  $T_r$ . Ambient temperature  $T_{amb}$  is measured in the nearby met-mast and the gearbox temperature  $T_g$  is estimated based on a 6 months monitoring campaigns which recorded the temperature of the gearbox wall facing the rear main bearing. (b) Simplified thermal circuit model of the drivetrain, which assumes that each 10-min instance reaches thermal equilibrium and average values of load, temperature and heat are estimated.  $\dot{Q}_r$  and  $\dot{Q}_f$  are the dissipated power by the main bearings. R represents the equivalent thermal resistance:  $R_1$  between front main bearing and ambient temperature;  $R_2$  between main bearings;  $R_3$  between rear main bearing and the ambient and  $R_4$  between rear main bearing and the gearbox closest surface to the main bearing housing. Other heat exchanges are not considered. The  $R_{(...)}$  are estimates on geometry of the drivetrain components (all assumed as steel) and bearings heat transfer coefficients suggested by Schaeffler TPI-176 (2014).

Preprint. Discussion started: 11 November 2025

© Author(s) 2025. CC BY 4.0 License.



300

305

310



To incorporate the life modification factor  $a_{\rm ISO}$  in the evaluation of the main bearings, estimates of the main bearings temperature are necessary, as the first is function of viscosity which is function of temperature. Figure 5a shows the estimated temperatures from the rear  $T_r$  and front bearing  $T_f$ , together with the measured temperatures, ambient  $T_{amb}$  and gearbox wall  $T_g$ . It is proposed to simplify the heat exchange between the heat dissipated by the bearings and the outer system (drivetrain), by assuming thermal equilibrium in each 10 min instance and thermal resistors, as shown in Figure 5b. The ambient temperature  $T_{amb}$  is measured by a spinner anemometer at the hub and the gearbox temperature  $T_g$  is estimated based on 6 month monitoring campaigns that recorded the temperature of the gearbox wall facing the rear main bearing. A SCADA-based small FNN model was trained to estimate values of  $T_g$  for each 10-minute instance, and it yielded 3 °C MAE, which is reasonable considering the scope of this investigation.

$$\dot{Q}_f - \frac{(T_f - T_{amb})}{R_1} - \frac{(T_f - T_r)}{R_2} = 0 \tag{17}$$

$$\dot{Q}_r + \frac{(T_f - T_r)}{R_2} - \frac{(T_r - T_{amb})}{R_3} + \frac{(T_g - T_r)}{R_4} = 0 \tag{18}$$

By applying the Kirchhoff circuit concept for thermal equilibrium, Equations 18 are obtained, which have two target variables,  $T_f$  and  $T_r$ . However, the dissipated power of a bearing is also affected by the bearing temperature (e.g.,  $\dot{Q}_f = f(T_f,...)$ ), as the latter influences the viscosity of the lubricant (the base oil of the grease). Because the variables depend on one another, the equations are coupled and cannot be solved explicitly. Instead, a Newton-Raphson solver was implemented in Python to iteratively estimate the results, and no convergence issue was encountered. This framework can be found in more detail in HIPERWIND D5.1 (2023). The dissipated powers were modeled as suggested by Schaeffler TPI-176 (2014), which separates them into two contributions: frictional heat driven by speed (and viscosity  $\nu$ ) and frictional heat driven by load. The grease has been assumed as Klüberplex BEM 41-301, a widely distributed industrial grease for wind turbine main bearings. Once  $T_r$  and  $T_f$  are estimated, the viscosity of the base oil is calculated according to ASTM D341-93 (1998). Lastly,  $a_{\rm ISO}$  can be calculated as a function of viscosity ratio  $\kappa$ , grease cleanliness level,  $C_u$  and  $P_{eq}$  as given by ISO-281 (2007).

# 5 Results

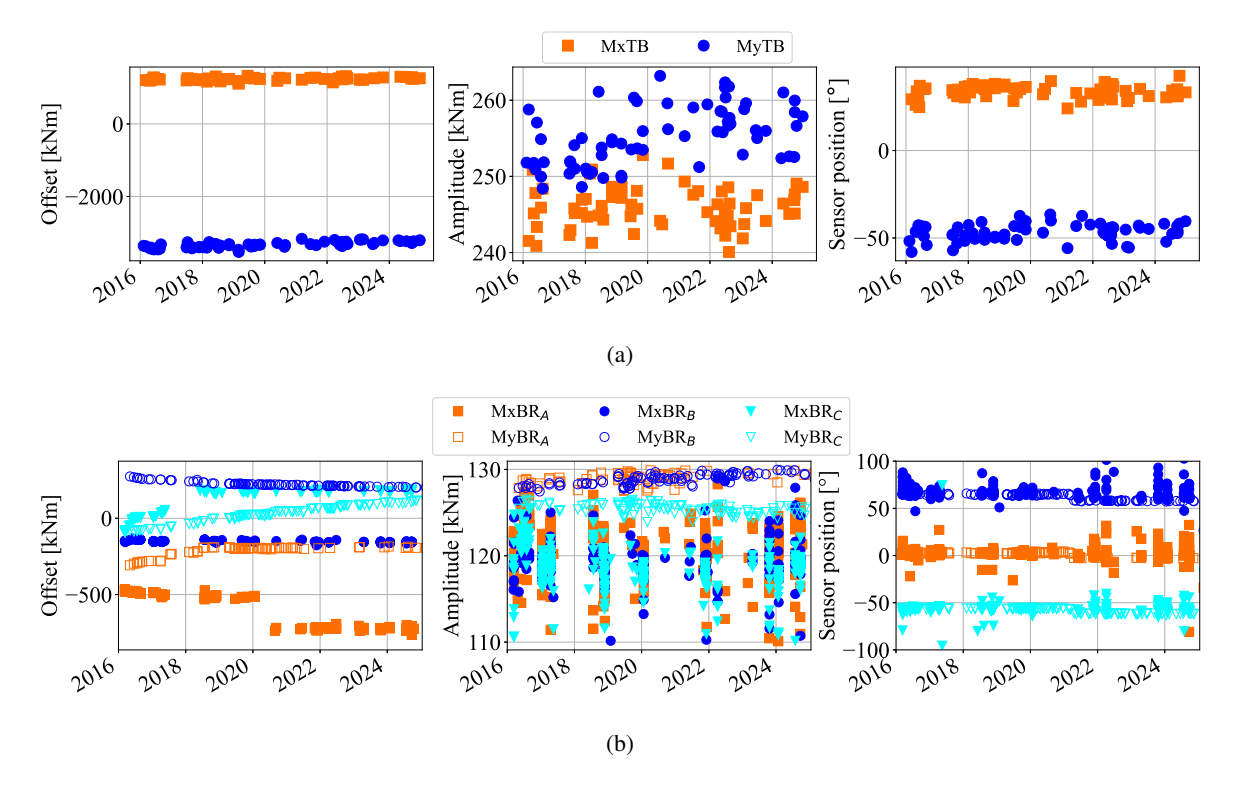
#### 5.1 Continual calibration routines

Figure 6 shows the identified calibration factors for each of the two tower bottom strain gauges and the six blade root strain gauges, all converted to bending moments as explained previously in Section 4.1. The charts to the right in both Figures 6a and 6b show the "Sensor position" represent the angle difference of the installed sensor with respect to the SCADA reference variable, the yaw angle  $\gamma$  for the tower (cardinal north as the zero point) and the azimuth angle  $\varphi$  for the blade sensors (blade A upward as the zero point). Automatic routines manage to identify the position of the sensors correctly with a standard deviation (std) of less than 4 degrees, even though the azimuth correction explained in the Appendix A was not applied at this stage, leading to higher variability before 2018 and after 2022.



330

From the left charts, it is possible to observe larger zero drifts for the blade root compared to the tower bottom strain gauges. The  $M_xBR_A$ ,  $M_yBR_A$ , and  $M_xBR_C$  also present an abrupt change in the zero drift in 2018 and 2020. This could be justified by sensor replacement or data acquisition settings; however, no final explanation has been validated. The amplitude in this method is the maximum gravitational overhang bending moment. In the case of the yaw sweep, driven by the rotor-nacelle weight in respect to the tower bottom, and for the LSI, driven by the blade weight in respect to the blade root. To have a quantitative accuracy quantification of the automatic routines in identifying the offset and the amplitude their unexplained variability are normalized by reference values: the mean  $M_{fore-aft}$  bending equal to 3540 kNm for the tower strain gauge and the mean  $M_{flapwise_{(A,B,C)}}$  bending equal to 500 kNm for the blade strain gauges, both at rated wind speed. From the middle chart in Figure 6a, an amplitude std of less than 4 kNm (equal to 0.04 MPa) can be observed for both sensors, which represents a variability of 0.1% to the tower reference. For the blade, an amplitude std less than 3 kNm, representing a 0.6% variability.



**Figure 6.** Identified calibration factors for a period of nearly 9 years, including offset, amplitude and sensor position. Each marker represents one identified yaw sweep for the tower bottom strain gauges and its calibration factors(a) and one Low-Speed Idling (LSI) for the blade root strain gauges and its calibration factors (b). In average, 2 calibration instances are available per month. The tower bottom sensors position is defined in respect to the yaw angle  $\gamma(t)$ . The blade root sensor position is defined in respect to the azimuth angle  $\varphi(t)$ .

Once the offsets, shown in the left charts, are used to remove the artificial zero drift from the sensors, there will still be residuals that are not explained by the automatic routine. The offset residuals of the tower showed a std of less than 60 kNm



350



(corresponding to 0.5 MPa), which is 1.6% of the reference. While, for blade strain gauges, the offset residuals had an std of less than 10 kNm, representing a variability of 2%.

#### 5.2 Lifetime of tower and main bearings

# 5.2.1 Fatigue damage accumulation

Once all strain gauges have been calibrated and high-frequency measurements and SCADA are available, the long-term lifetime can be estimated over time, as shown in Figure 7. Considering that failure is reached at unity, the basic lifetime of the main bearing  $L_{10}$  can be evaluated using Equation 7. The front bearing  $L_{10,f}$  is 166 years and the rear bearing  $L_{10,r}$  is 333 years. Similarly, the tower has a even larger lifetime of 1770 years. This significantly longer lifetime, compared to the design lifetime of 20 years proposed by IEC 61400-1 (2019), is in part justified by the low wind potential of the Risø site, as discussed in Section 3. However, it also points to the fact that older and smaller turbines, such as the DTU research V52 turbine, have long remaining useful lifetimes (RUL) of key components that should be considered in lifetime extension (LTE) decisions.

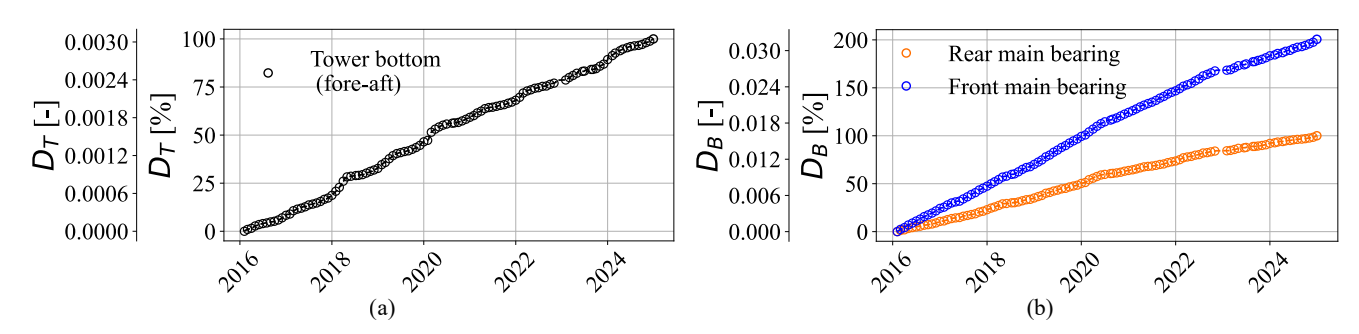


Figure 7. Fatigue damage accumulation of (a) the tower (structural component) and (b) the main bearings (rotating components) of the DTU research V52 turbine for 9 years. Fatigue damage was counted according to Equations 2 and 7. Charts have an absolute accumulation and a normalize y-axis in respect to the end measured accumulated damage (normalization of  $D_B$  considers the rear main bearing).

#### 345 5.2.2 Linear zero-drift assumption and simple uncertainty propagation to tower and main bearing lifetime.

It is proposed to assume linear zero drift of the different strain gauges as a single linear function or a combination of linear functions, which can be derived from continuous calibration factors over time. Then it is important to quantify the uncertainty of this assumption in the life of the main bearings, which is based on the absolute load values P. Figure 8 shows how this analysis was carried out to evaluate the effect on main bearing basic rating life  $L_{10}$  as described by Equation 6. Representative 10-min instances (DLCs 1.2, 3.1 and 4.1) were used to estimate the main bearing rating lifetime  $L_{10,j}$  assuming a offset with Gaussian distribution. Then 10000 Monte Carlo iterations were carried out. For all three instances, the std of both bearings  $L_{10,j}$  was below 0.7%. Similar analysis was carried out for the fore-aft fatigue load. However, fatigue is not affected by the mean load value (as described in Equation 2 and is then not sensitive to the offset, assuming there are no large yaw angle variations within 10 min instances, see Equation 9.

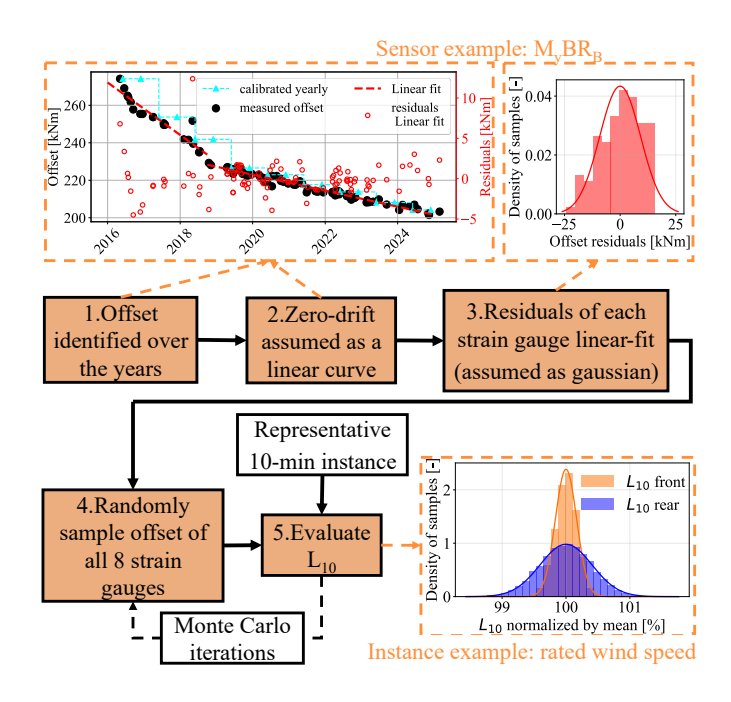


Figure 8. Uncertainty quantification flowchart to estimate the variability in the main bearings basic lifetime  $L_{10,j}$  in a 10 min instance j due to the linear assumption of the zero-drift strain gauges once continual calibration is applied. Each strain gauge offset is randomly sampled from its deterministic linear fit and the residuals distribution. Monte Carlo is applied for 10000 iterations.

# 355 5.2.3 Effect of periodic calibration on the main bearings $L_{10}$

Now that continuous calibration with linear zero drift has been defined as the benchmark with a error less than 1%, it is sought to understand how periodic calibration of strain gauges, as often carried out in the industry, could affect the lifetime estimation of the main bearings. Table 2 shows the difference between the  $L_{10}$  measured over 9 years with continual calibration compared to the periodic calibrations carried out. The absolute results of  $L_{10}$  error due to calibration periodicity are not generalizable, as they are influenced by the zero drift behavior of each monitoring setup and the absolute loads of the wind turbine. However, it highlights how severely poor strain gauge calibration can influence the lifetime estimation of main bearings.

**Table 2.** Error in the  $L_{10}$  estimation for 7.5 years as a function of how often strain gauges are calibrated.

	Monthly	3-months	6-months Yearly 2-year 4-years		4-years	At commissioning	
$L_{10}$ error [%]	8.0	9.3	11.9	13.1	34.8	70.5	90.6

# 5.3 Virtual load sensor performance validation

More than 160 h of training data were used, as no significant improvements were found by enlarging the dataset, while down-sampling from 50 Hz to 10 Hz remained within the error convergence. The latter could decrease the dynamic content and







380

385

underestimate the measured fatigue damage; therefore, to verify this, a procedure proposed by D'Antuono et al. (2023) was carried out, and sampling frequencies lower than 8 Hz contained more than 98% of the measured fatigue damage in representative instances, to all considered design load cases (DLCs). A sampling frequency of 10 Hz is used.

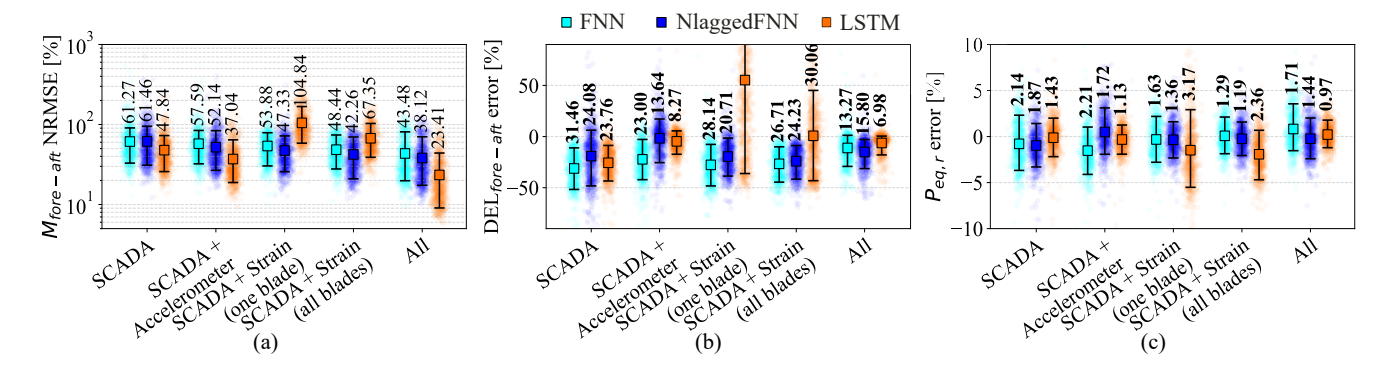


Figure 9. Virtual load sensor validation performance applied to 160 hours. Their performance is shown based on the 3 metrics described in Equations 15 and 16. The different columns represent the feature selected as inputs and the different colors the model type (neural network architecture). The box-plots show the mean value and the  $10^{th}$  and the  $90^{th}$ . The number in the left subplot are the mean value of the NRMSE, whereas the bold values in the middle and right subplots, have the mean absolute error (MAE).

The 15 different combinations of virtual load sensors (5 input options and 3 model types) are validated using 160 h from the 2019. From left to right, Figure 9 presents all combinations of models tested in terms of the metrics shown in Equations 15 and 16: including NRMSE  $M_{fore-aft}$  (a), MAE  $DEL_{fore-aft}$  (b), and MAE  $P_{eq}$  (c). Raw data are added for completeness as transparent markers. It can be seen that the LSTM model with "All" inputs outperforms the other models significantly when comparing NRSME. The mean error of 23.41% is almost half the second-best performing model combination (LSTM and "SCADA+Accelerometer"), which yields 37%. However, when no accelerometer signal was included and blade strain gauges were added, the LSTM performance worsened compared to the FNN and NlaggedFNN models. It seems that LSTM cannot attenuate the pronounced 1P, 2P, and 3P contributions of the blades, without a clear estimate of the first fore-aft frequency component (present in the accelerometer signal). Regarding the equivalent load of the main rear bearing  $P_{eq,r}$ , influenced by the thrust estimate from the virtual load sensors, it is observed a overall negligible difference between all combinations of models. Models using only "SCADA" already reach MAE errors below 2%. The same results were found for long-term deployment over 7.5 years, all models within 2% of main bearing  $L_{10}$  estimates.

For the equivalent damage loads at the tower bottom fore-aft  $DEL_{fore-aft}$ , models solely using SCADA had a minimum MAE error of 23.76%. Looking at Figure 10, it can be observed that the model with SCADA (LSTM) had an overprediction for very low amplitude cycles, while underprediction for larger amplitude cycles. This becomes more predominant for above rated wind speed conditions (refer to Figure 10b). Looking at its PSD, the model also does not properly capture the frequency components of the reference signal  $M_{fore-aft}$ . Adding the accelerometer yielded strong improvements. The best performing combination with "SCADA + Accelerometer" and LSTM had an MAE of 8.27%, very close to the overall best performing combination of "All" and LSTM with 6.98%.







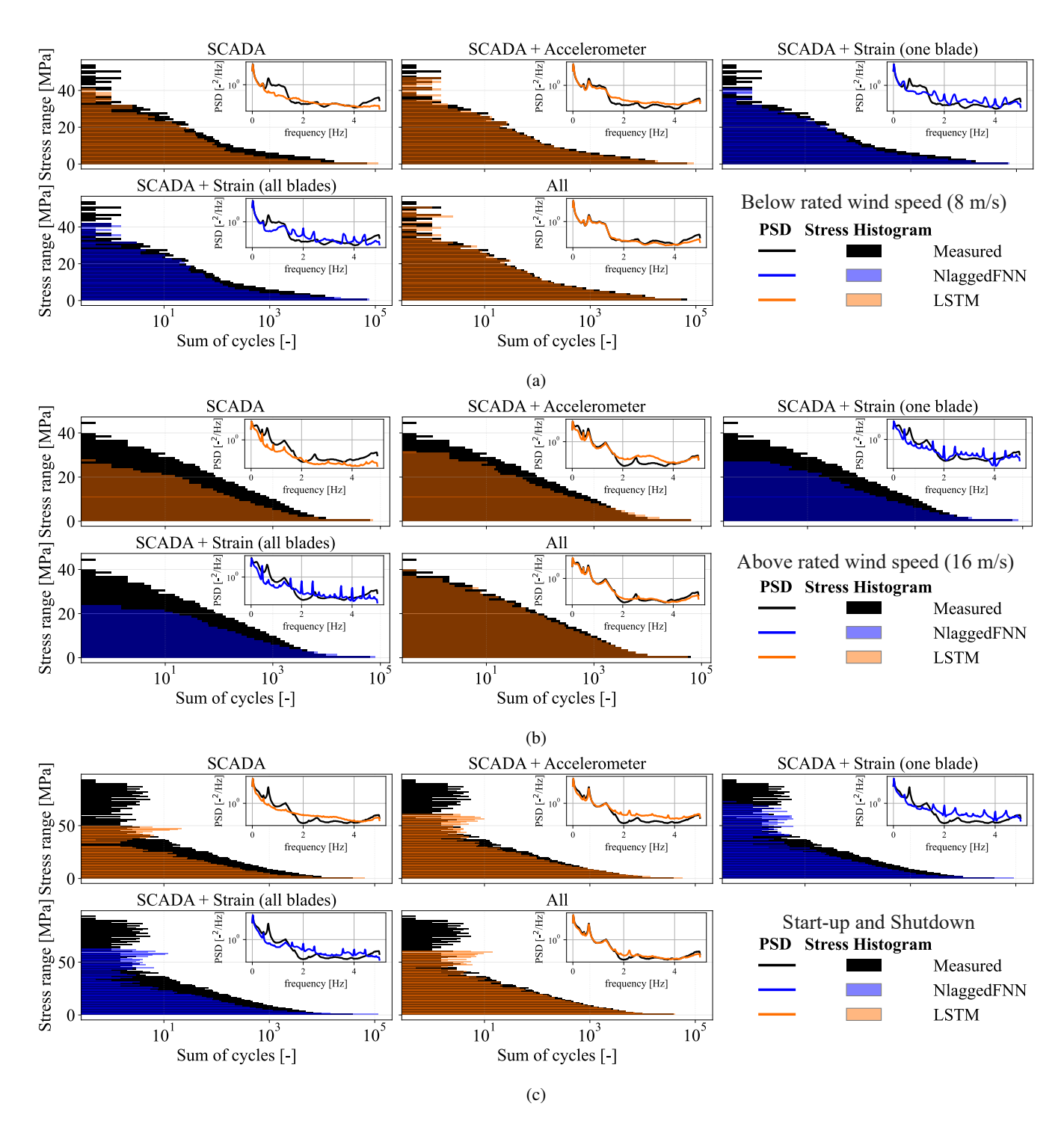


Figure 10. Stress cycle histogram and Power Spectrum Density (PSD) chart (inset top right) of tower bottom  $M_{fore-atf}$  estimate for the different input signal combined with their best performing model compared to the measured (black). All stress histograms are the summation and the PSD charts the averaging of 100 instances from 2019. (a) Below rated wind speed 8 m/s (DLC 1.2). (b) Above rated wind speed 16 m/s (DLC 1.2). (c) Start-up and shutdown (DLC 3.1 and 4.1)





395

400

405

The models that included strain without accelerometer have a worsened performance of 20.71% and 24.23% for the best combination with NlaggedFNN, and also included undesired, sharp and narrow-band peaks, most likely coming from the blade modes, that are not transmitted to the tower in reality. Looking close to the two best performing model combinations overall, "SCADA + Accelerometer" and "All" with LSTM, it is worth taking a closer look at Figures 10a and 10b. It is observed that only the model "All" is consistent in predicting stress ranges at both below and above rated wind speed, while rarely overpredicting the energy content for frequencies components above 0.62 Hz. Figure 10c shows the models performance under DLC 3.1 and 4.1 together. Again, LSTM with "All" shows the most consistent results. However, all the possible combinations under-predict large oscillations, and consequently large stress ranges.

#### 5.4 Tower fatigue estimation using virtual load sensors

LSTM is chosen as the best model to combine with "SCADA", "SCADA + Accelerometer", and "All", while NlaggedFNN is chosen for "SCADA + Strain" (one and all blades). The long-term deployment of these is then performed to verify their reliability in estimating the lifetime of the tower. Unfortunately, since the high-frequency database before July 2017 is sampled at 35 Hz, in contrast to 50 Hz after July 2017, the results related to the implementation of virtual load sensors do not include this initial period, as the models were trained on 10 Hz data. Downsampling 35 Hz to 10 Hz requires interpolation rather than a clean decimation (50 Hz to 10 Hz), which may affect consistency. Figure 11 shows the accumulated tower fatigue damage of each virtual load sensor combination  $D_T$  normalized by the final accumulated damage measured. It is interesting to note that more damaging contributions are present at the beginning of each year because the Danish winter has higher wind speeds. In terms of virtual load sensors, all have underpredicted the accumulated damage (under-conservative), which is expected looking at the analysis done during validation and shown in Figure 10. The difference between the best-performing model "All" and the second model "SCADA + Accelerometer" is equal to 11%, from 64% to 75%. The remaining three models perform considerably worse in the long term with estimates below 30% of the reference damage.

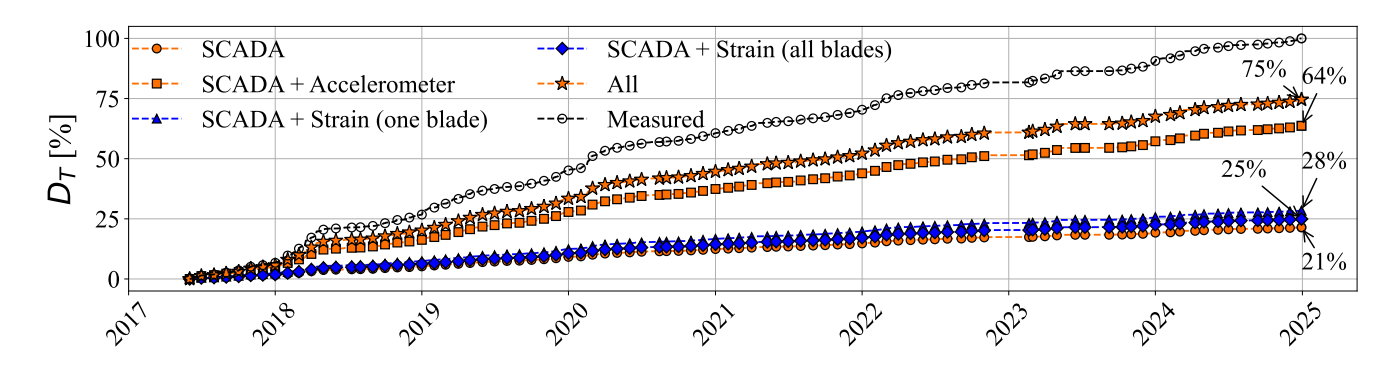


**Figure 11.** Tower bottom fore-aft fatigue damage accumulation comparison between different virtual load sensors models. It shows the total accumulation for a period of 7.5 years normalized, for the sake of comparison, by the final measured fatigue accumulated damage. The different model combinations are shown by inputs used (marker) and by model type (marker fill color). The latter for sake of consistence maintains the colors from Figure 9, blue for NlaggedFNN and orange for LSTM.



425



# 5.4.1 Proposed experimental slope correction for tower damage accumulation and statistical uncertainty

If a virtual load sensor is consistent throughout the majority of operating conditions over the year, it would underestimate different years with a similar error. Figure 12a shows the comparison for a full year (2018 as the first round year available) of estimated and measured accumulated damage. The slope  $\eta_k$  represents the under-prediction ratio, calculated as the linear fit slope between the estimate and the measured accumulated damage yearly. And the greater the linear fit coefficient of determination  $R^2$ , the lower the unexplained variability of the linear fit of a given virtual load sensor. Then, one could have an accumulated damage from the virtual load sensor adjusted by the yearly slope as in

415 
$$D_{T,a} = \frac{D_{T,vls}}{n_{l}}$$
 (19)

where  $D_{T,vls}$  is the original and  $D_{T,a}$  is the adjusted accumulated damage of the virtual load sensor. The slope  $\eta_k$  is the linear fit slope between the virtual load sensor and the measured damage for a given year k, and it is used as a correction factor.

An issue with the proposed experimental correction is the error associated with the choice of a given year k to calculate the slope by chance. Figure 12b shows the calculated  $\eta_k$  for each year independently. The "All" and "SCADA + Accelerometer" models have the slope closest to unity for all years compared to the remaining models, while the first has the lowest variability. Figure 13 then attempts to evaluate the uncertainty by individually calculating the slope correction factor for each year of the 7 years available and adjusting the expected accumulated damage of the two best performing virtual load sensors by the average slope  $\eta_{avg} = 1/N \cdot \sum_{k}^{N} \eta_k$ , where N is the number of years. According to Schillaci (2022), to reach an estimate standard deviation (std) accuracy of  $\pm 10\%$  with limited samples with confidence 90%, more than 100 samples are required, considering a Gaussian distribution. Since our available N is low (7 years), both the (std) and the maximum/minimum bounds are evaluated.

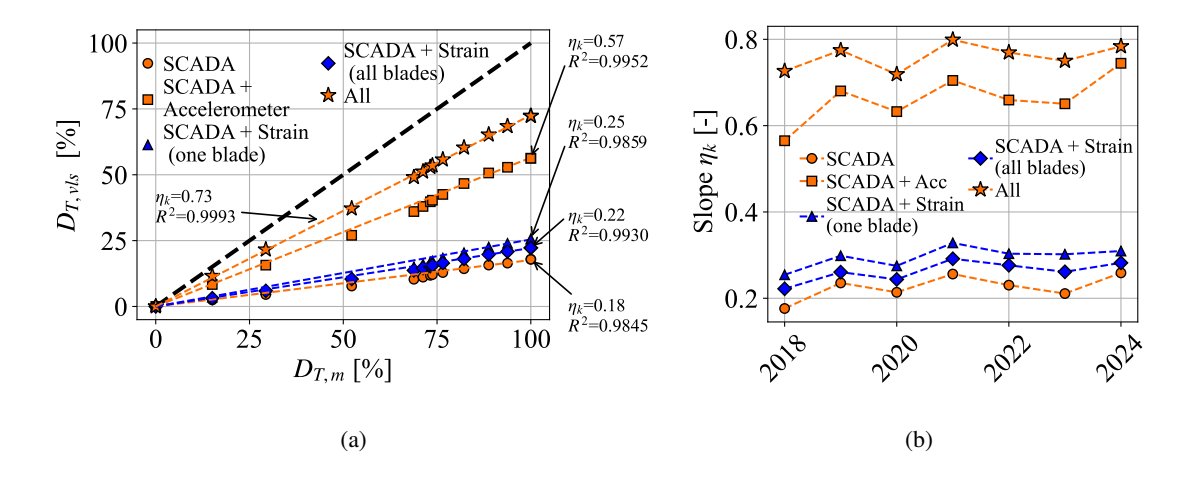


Figure 12. (a) Comparison between accumulated damage from virtual load sensors  $(D_{T,vls})$  and measured  $(D_{T,m})$  for 2018. The slope  $\eta_k$  of each model refers to the linear fit slope, while "R<sup>2</sup>" refers to the coefficient of determination (markers are shown once per month). (b) The slope  $\eta_k$  calculated for each full year k. Blue for NlaggedFNN and orange for LSTM.



435



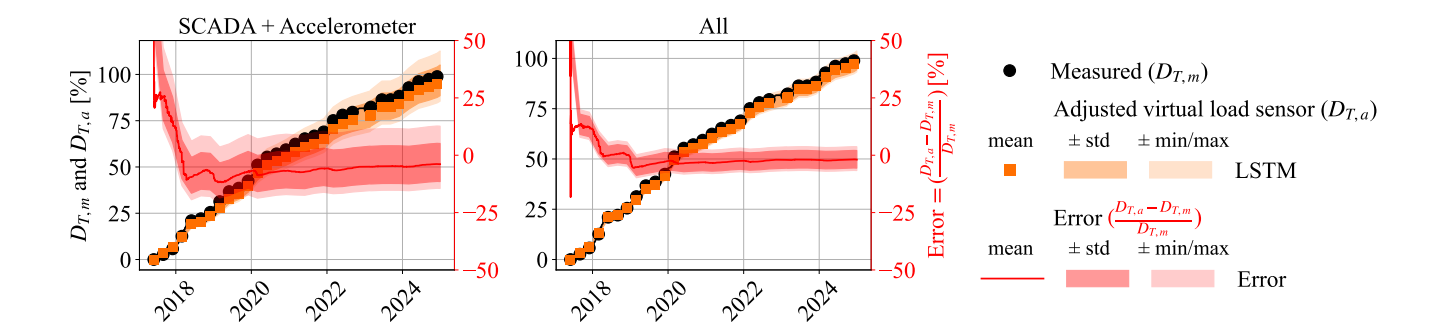


Figure 13. Measured  $D_{T,m}$  and adjusted  $D_{T,a}$  damage accumulation of the virtual load sensors based on the yearly slope correction are shown. Only the two best performing models are shown. The adjusted damage by the average slope value for the 8 years is shown as the markers. The filled areas represent the variation around the standard deviation (inner) and bounded between the maximum and minimum possible values observed (outer). The error between virtual load sensor and measured damages accumulation in shown on the right red y-axis.

It can be said that the model "All" with LSTM has the shortest error convergence time nearly within 6 months, and has a mean error for the adjusted accumulated damage equal to -1.8% and variability within 3.5% and -6.5%. The second best performing model "SCADA + Accelerometer" with LSTM has a mean error of -4.2% and a variability bounded within 13% and -15%. The remaining virtual load sensors are also shown, but should not be considered as reliable as the latter, since these do not capture neither the PSD nor the stress ranges distribution in a consistent manner. In other words, the final damage will match but with a very different estimated  $M_{fore-aft}$  signal compared to the measured.

#### 5.5 Main bearings loads and fatigue lifetime analysis

As detailed in Section 2.2, the main bearing life is calculated directly from the applied radial and axial loads. The axial load of the main bearing  $F_a$  is linearly linked to the tower bottom bending moment as in  $F_a = M_{fore-aft}/h$ , where h is the height difference between hub height (44 m) and the height of the sensor (3.787 m). Here,  $M_{fore-aft}$  is assumed to be representative of the turbine thrust curve. The radial load of the main bearings  $F_r$  is equal to the estimated  $R_f$  (front) and  $R_r$  (rear), respectively. For a more detailed explanation, see Sections 3 and 4.2. The 10-min mean loads are shown in Figure 14 as a function of wind speed. The front and rear bearings  $F_r$  have different behavior with respect to the wind speed. The front main bearing has a fairly flat distribution at higher load, while, for the rear main bearing, the radial load is incremental. The  $F_a/F_r$  ratio for the rear main bearing is almost in its entirety above the limiting factor, which will worsen the estimated rating life, as the Y factor increases (see Equation 4). Finally,  $P_{eq}$  of the front bearing has a slight positive trend, most probably due to higher rotor speeds with higher wind speed, while the rear bearing's dynamic equivalent load is driven by the axial load  $F_a$ .





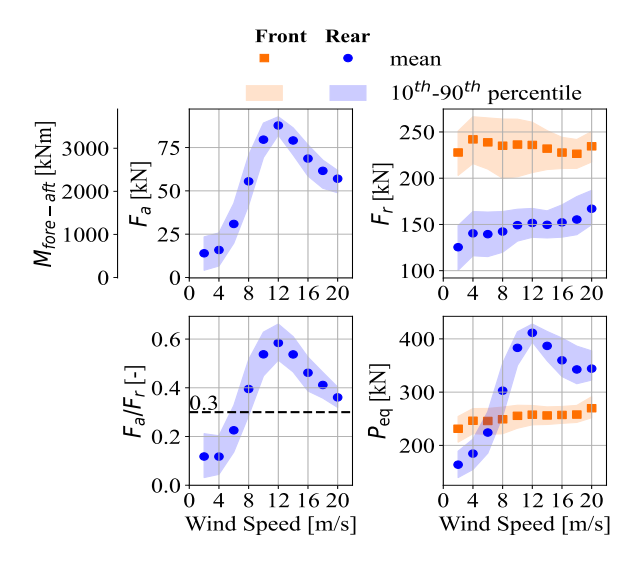


Figure 14. Front and rear main bearing loads as function of the wind speed. The obtained axial load  $F_a$  radial as function of the tower bottom bending moment  $M_{fore-aft}$ , the radial load  $F_r$ , the ratio with the rear bearing limiting factor, and the dynamic equivalent load  $P_{eq}$  are presented. The 9 years mean value is represented by the marker while the  $10^{th}$ - $90^{th}$  percentiles by the filled area.

#### 5.5.1 Sampling frequency and gearbox mounting stiffness assumptions

Before moving on to the long-term results, it is important to verify some of the assumptions made in this work. As in the fatigue estimation of the tower bottom, the  $P_{eq}$  and the  $L_{10}$  were calculated based on a downsampling of the measured data from 50 to 10 Hz. Figure 15 shows the effect of this assumption on the estimated loads, as the variation from the estimated downsampled load less the measured load at 50 Hz (normalized). It seems fair to conclude that at 10Hz, there will be a mean error of less than 2% with a  $10^{th}$ - $90^{th}$ , within 5%.

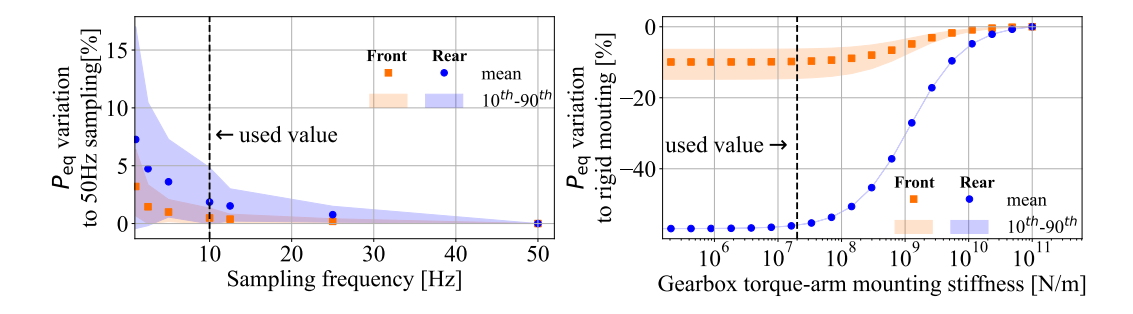


Figure 15. Results of sensitivity analysis of 160 h data on the main bearings dynamic equivalent load  $P_{eq}$ ; left: influence of sampling frequency of measurements; right: influence of stiffness of gearbox mounts. The used value for the gearbox mounting stiffness refers to the literature values found in Haastrup et al. (2011) and Keller et al. (2016).





On the other hand, the assumption on which stiffness should be used to model the gearbox mounting fixation points into the bedplate has been shown to be one order of magnitude more relevant. In the right subplot of Figure 15, nearly 10% and 60% overprediction of the front and rear dynamic equivalent loads  $P_{eq}$  could be reached, if a gearbox is assumed to be rigidly fixed in a 4-point drivetrain, see Figure 3.

# 5.5.2 Environmental and operational conditions (EOCs) mapping of the main bearings dynamic equivalent loads $P_{eq}$

Having 7.5 years of the main bearing  $P_{eq}$  available, it was possible to couple such values with the environmental conditions of each mean 10 min instance to visualize potential patterns. Figure 16 confirms the intuitive reasoning that the equivalent loads of the front main bearing  $P_{eq,f}$  are driven more by the static gravitational load of the rotor. However,  $P_{eq,f}$  still contains almost 10% fluctuations due to the shear exponent from 0.05 to 0.15 in all wind ranges and a similar turbulence effect at the rated wind speed. In a different manner, for the rear main bearing, the turbine thrust curve dictates the value of  $P_{eq,r}$ .

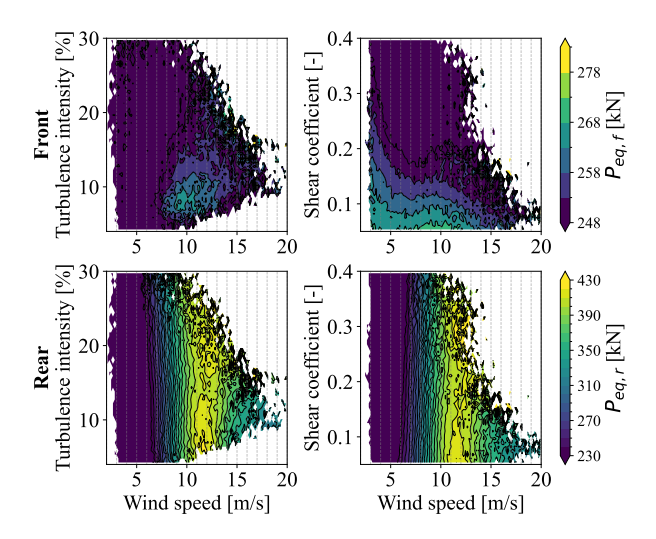


Figure 16. Equivalent dynamic loads of the front  $(P_{eq,f})$  and rear  $(P_{eq,r})$  main bearing mapped as function of wind speed, turbulence intensity and shear exponent. The measurement period covers from July 2016 to July 2024 (included).

Looking closely at  $P_{eq,f}$ , the results fairly resemble Kenworthy et al. (2024) for a 3-point drive train for the effect of lower shear on increased bearing loads. However, a more substantial effect of low turbulence is found at the rated wind speed, which is comparable and can exceed the shear influence, as also suggested by the HIPERWIND D5.4 (2024) report. An increase of 10% of  $P_{eq,f}$  loads (from 248 to 268 kNm) can be seen in the rated wind speed for the turbulence values of 15% to 10%. A similar load increase is observed for shear exponents of 0.15 to 0.08 at rated wind.

In terms of the load on the rear main bearing  $P_{eq,r}$  (locating), in addition to the dominant influence of the mean wind speed in general, the effects of turbulence are similar to the main front bearing at the rated wind speed. Approximately 10% increase in load driven by a change in turbulence from 15% to 8%. Although shear also has an influence on loads, it is to a lesser extent.



475



Important to note, the discussion above does not imply an overall longer or shorter lifetime of the main bearing, as Figure 16 zooms in on the most damaging environmental combinations and disregards, for example, the effect of shear and turbulence at smaller loads, as the color bar was limited to focus on higher loads ( $50^{th}$  percentile minimum). The goal is to discuss possible load reductions in the case of more damaging conditions.

#### 5.5.3 Main bearing lifetime using thrust estimate from virtual load sensors

The application of virtual load sensors as a thrust estimate and then the axial load of the rear main bearing resulted, for all models, in an estimation error of  $L_{10,r}$  around 10% for 7.5 years. The model with only "SCADA" with LSTM was the best performing model. This might come from the fact that the main bearing loads, and, consequently, their useful life, are not affected by the dynamic component of the axial load, but only by the mean load level. In this manner, there was no significant performance difference between deploying the different virtual load sensors, in agreement with the results in Figure 9(c).

# 5.5.4 Main bearings modified rating life: $L_{10m}$ and $a_{ISO}$

Applying the drivetrain thermal model, consistent temperature ranges were found for the normal operating conditions (DLC 1.2) of the main bearings. The temperatures of the front and rear main bearings had maximum values of 55 and 61  $^{\circ}$ C, respectively, while  $\kappa$  (viscosity ratio) had minimum values of 0.84 and 0.64 respectively.

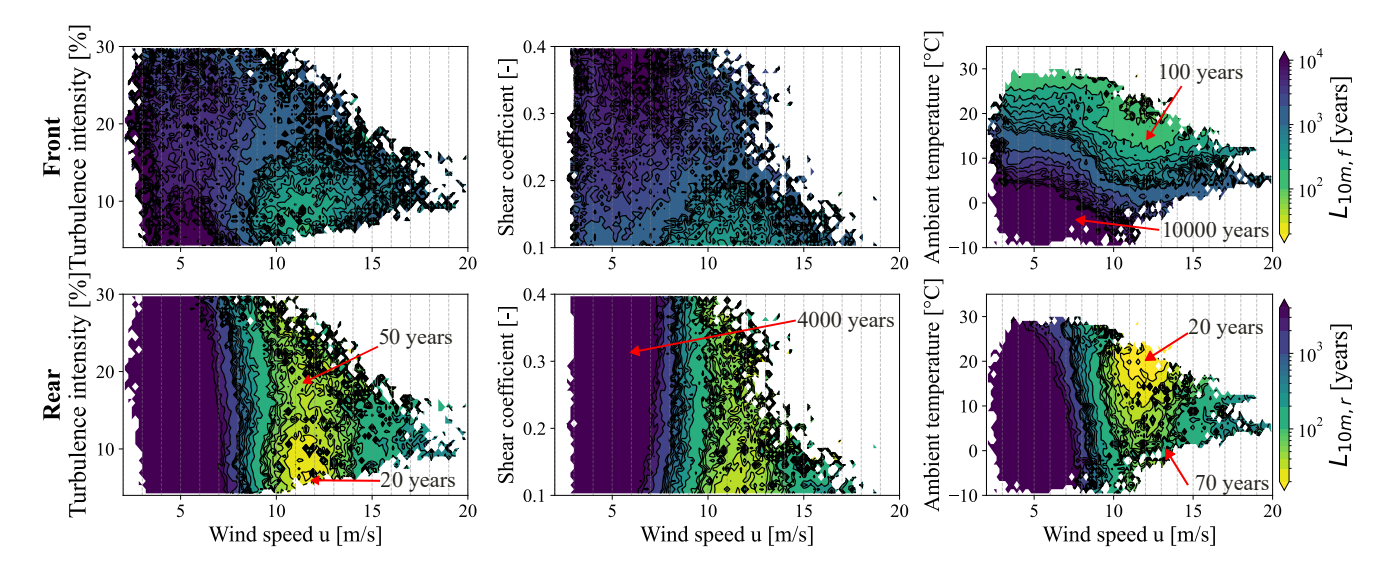


Figure 17. The modified rating life of the front  $L_{10m,f}$  and rear  $L_{10m,r}$  main bearings of the DTU research V52 turbine is mapped as function of relevant environmental conditions. It is assumed a severe level of contamination for the grease lubricant. The latter represents a scenario in which re-greasing intervals recommended by the OEM are not followed. Important to note that there are limits related to  $a_{\rm ISO}$  implementation as defined by ISO-281 (2007): at  $a_{\rm ISO} = 50$  and at  $e_c C_u/P_{eq} = 5$  (maximum bound) and at viscosity ratio  $\kappa = 0.1$  (minimum bound) which has not been reached in this work. The lower limit of the color bar (yellow color) was chosen to match the turbine design lifetime of 20 years. The measurement period covers from July 2016 to July 2024 (included).

490

495

The seasonal variation corresponded to approximately  $\pm 10$  °C in the front bearing and  $\pm 8$  °C in the rear bearing temperatures, while the operational variability reached around  $\pm 15$  °C variation in the front and  $\pm 20$  °C in the rear bearing temperatures. The results of such environmental and operation conditions (EOCs) can be visualized in Figure 17, assuming a severe level of grease contamination. The grease cleanliness affects the parameters to estimate the variable contamination factor  $e_c$ , which by consequence affects the  $a_{\rm ISO}$  (see ISO-281 (2007)). This assumption represents a worse scenario in which re-greasing of the main bearings is not performed in the long-term as suggested by the manufactures. It highlights the large impact of the ambient temperature on the modified rating lifetimes of main bearings in which there is no nacelle temperature control. For the rear main bearing, even for such an overdesigned bearing, at rated wind speed and ambient temperatures above 20 °C, the bearing lifetime is reduced to below the design lifetime of 20 years. In addition to that, once  $a_{\rm ISO}$  is considered, it seems that turbulence overcomes shear as the most influential factor for the rear main bearing at the rated wind speed.

Even though significant variations can be observed on the  $L_{10m}$  due to EOCs, it is important to mention that the grease cleanliness level affects the bearing lifetime more severely. A severe level of contamination could be reached at the end of the design lifetime in case no periodic re-greasing are carried out, as described by ISO-281 (2007). However, there are better and worse scenarios. Figure 18 shows in a log scale the distribution of  $a_{\rm ISO}$  as function of the grease cleanliness assumed or inspected in a wind turbine. In the worst case scenario with "very severe contamination" around 70% of instances are penalized and  $L_{10m,r}$  goes from the initial  $L_{10,r}$  of 315 years to 130 years lifetime, more than 50% lifetime reduction.

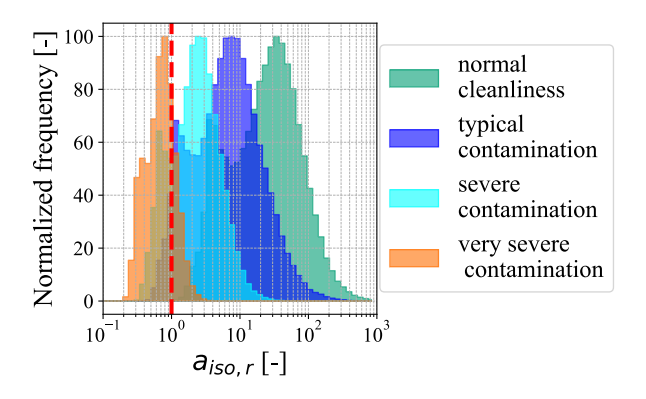


Figure 18. Normalized histogram showing the distribution of the rear main bearing life modification factor  $a_{ISO,r}$  as function of the grease cleanliness levels. The red dashed line shows the limit for  $L_{10} = L_{10,m}$ . The bound of  $a_{ISO} < 50$  is not applied for the sake of clarity.

# 6 Discussion

500

The assumption that the strain gauge zero-drift in a wind turbine tower and blade follows a linear curve might be an oversimplification. Many factors can influence the zero drift of the strain gauges. As described by Hoffmann (1989), the measuring grid has its own fatigue deterioration, the adhesive can wear over time, and the bending of the connecting wires and several impurities (e.g., mold) that can add unwanted electrical resistance to the circuit over time. However, it is interesting to observe

Preprint. Discussion started: 11 November 2025

© Author(s) 2025. CC BY 4.0 License.



505

510

515

520

525

530

535



that eight independent strain gauges from the DTU research V52 turbine have presented similar behavior over time, with low unexplained variability after the proposed correction. Similar variability was also found for a 5 MW offshore turbine in Faria et al. (2025). The larger variability from the blade root strain gauges calibration factors could be explained by the fact that its Wheatstone bridge is compensated for temperature differences in the whole blade, but not for temperature gradients between the two blade surfaces. It would be interesting to see if this result holds in more case studies.

One last detail worth mentioning about the strain gauge methodology is that the configuration of the Wheatstone bridge chosen to measure bending moments will highly affect the reliability of the sensors output. The full bridge of the blade root strain gauges was not inherently compensated for temperature gradients between the blade faces, differently from the full-bridge of the tower bottom strain gauges. Because of that, the residuals had a small seasonality effect present. So, temperature effects can also add variability and bias to the zero drift of strain gauges.

In terms of virtual load sensors, it was a methodological decision to use k-means to select and generate training and validation datasets. Rather than a more generalizable conclusion usually sought by methods such as the Latin-Hyper cube, the goal here was to test and deploy the best-performing model for the long-term monitoring of the DTU research V52 turbine, as it is rare to find similar results in the literature. The performance of the virtual load sensor for DEL estimation is worse than that found in works such as de N Santos et al. (2024). The addition from the present work comes from the deployment of long-term and time series virtual load sensor. In which it is interesting to highlight that a mere 1% difference in MAE DEL between models led to a 11% difference in the lifetime estimation. The experimental slope correction results should not be seen as fully validated, but as a trial to adjust models that consistently capture the dynamic content of the tower bottom while underpredicting the peaks and valleys, leading to constant stress range underprediction. Using in this work 7 years of measurements showed very low variability, within around  $\pm 5\%$  for the best performing model (LSTM with "All" inputs). More advances in machine learning models and training techniques could still be tried.

Regarding monitoring the bearing lifetime, it was interesting to observe that the initial gearbox assumption could lead to large errors in the estimation of the lifetime of the components. The stiffness of the gearbox mounting could lead to an error of 60%  $P_{eq}$ , which, due to the bearing exponent p equal to 10/3, would mean underestimating the lifetime  $L_{10}$  by 198% for the location of the main bearing.

The lifetime estimate of the main bearings was an order of magnitude higher than the required lifetime of 20 years, making it less probable to fail due to rolling contact fatigue in the DTU research V52 turbine. However, mapping of their loads facing key environmental conditions can provide more generalizable lessons on how to operate and maintain such expensive components in the long term for other turbines with similar drivetrain setup. At a wind farm level, if farm power curtailment is required, turbines with low inflow turbulence could be prioritized to be curtailed to have a more significant reduction of main bearing loads. In contrast to what one would intuitively expect in the field of wind energy research, lower intensities of turbulence could penalize the useful life of the main bearings, as also shown in HIPERWIND D5.4 (2024). In fact, good estimates of operating temperature and grease cleanliness were identified as key drivers in the estimation of main bearings lifetime. Although the thermal model resulted in realistic temperature ranges, validation with measurement values is the logical next step.

Preprint. Discussion started: 11 November 2025

© Author(s) 2025. CC BY 4.0 License.





#### 7 Conclusion

550

555

560

In this work, methods were investigated to allow for reliable lifetime counting of large load-carrying components, both structural in the form of a tower and rotating in the form of main bearings. The work was validated on the DTU research V52 wind turbine for a continuous period of almost a decade.

From the proposed research questions that guided this study, the main learnings and possible limitations are as follows.

- The strain gauges at the bottom of the tower and the root of the blade were continual calibrated for 9.5 years with at least 20 calibration instances per year. The yaw sweeps and Low-Speed Idling (LSI) routines were verified for long-term calibration, and all strain gauges presented reliable behavior. We assumed linear behavior to model the zero drift, which has to be validated by carrying larger case-study comparisons.
- Lifetime counting of a structural component, such as the tower, and other load-carrying components, such as main bearings, was carried out for almost a decade, without having design information from the blade or mid-fidelity aeroelastic models in hands. Attention should be paid to the quality of SCADA sensors and drivetrain modeling assumptions.
  - The use of virtual load sensors based on data-driven methods is promising in the field of wind energy, where Structural Health Monitoring (SHM) campaigns can be expensive and take a long time (even more for offshore assets). These could serve as a continuous high-frequency thrust estimate. In this work, the counting of 7.5 years of the fatigue lifetime of the tower bottom using a virtual load sensor yielded in its best model a prediction of damage of 75%, and after an experimental correction, assuming a year of available measurement data, ±5 % lifetime error. However, in the field of data-driven methodologies, there are many models, training techniques, and deployment cases that could bias the results. For this reason, the results from this work might not be seen as the state of the art or entirely generalizable but as a discussion on the challenges of applying and validating virtual load sensors on operating wind turbines considering several DLCs.
  - Finally, the main bearings loads  $P_{eq}$  and modified lifetime  $L_{10,m}$  were mapped in terms of relevant environmental conditions and grease cleanliness. The first showed that a front main bearing in a 4-point drivetrain has longer life by a higher shear exponent, whereas the rear main bearing, at rated wind speed, has higher loads for lower turbulence intensities. Neglecting the stiffness of the gearbox mount renders unrealistically high  $P_{eq}$ , but having the stiffness values within realistic ranges results in little influence on the lifetime. Finally, ISO-281 (2007) life corrections for lubricant cleanliness result in significantly different lifetimes but are not validated for large grease-lubricated bearings. Future research might focus on establishing these factors with bearings and lubricants typically used in wind turbines.



575

580



# Appendix A: Azimuth angle correction for the DTU research V52

Figure A1 presents the problem and the solution applied for the azimuth angle sensor. For periods before 2018 and after 2020, the measured azimuth angles contained severe variations in regular patterns, which did not extend to variability in the edgewise bending moment  $M_{edgewise}$  of the blades. In this manner, such variations were triggered as a sensor malfunctioning.

To correct for such an issue, an azimuth angle estimate  $\varphi_e$  was derived as a constant-gain blend between two complementary signals. The first signal is the measured azimuth angle  $\varphi_m$  sampled at 10 Hz, shown in Figure A1 as the black line (left y-axis). The second signal is the controller-defined rotor speed (SCADA)  $\omega$  sampled at 10 Hz, which has a lower resolution, and shown in the same figure as the red line (right y-axis). The period  $\Delta t$  is defined as the inverse of the sampling frequency.

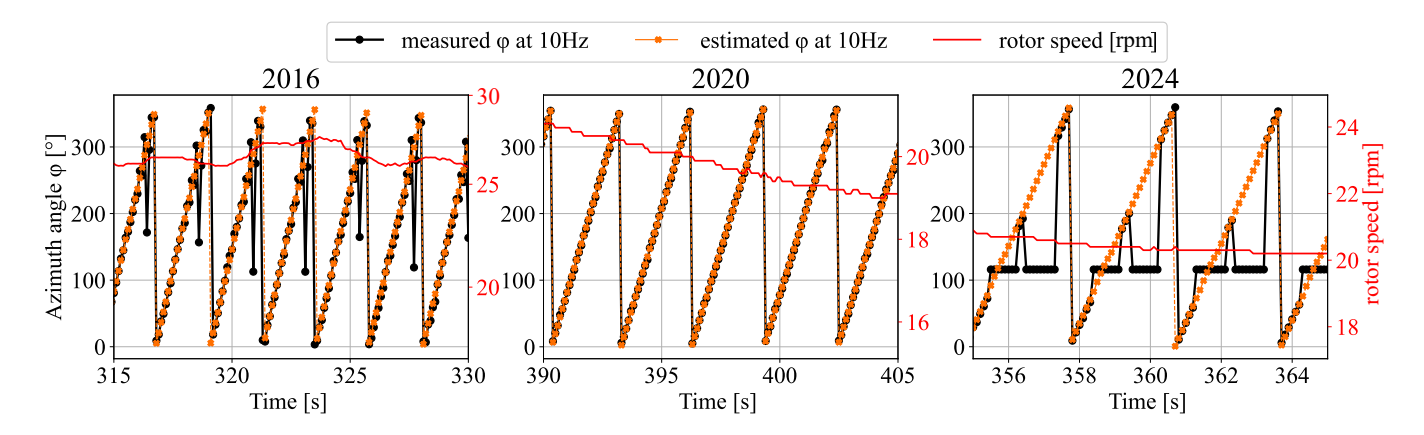


**Figure A1.** Representative examples of the azimuth angle in the SCADA from the DTU research V52 turbine showing problems with the measurement data acquired in 2016 and 2024. An estimated azimuth angle (orange) is performed based on the controller SCADA rotor speed (red) and the measured azimuth angle (black).

The correction method works by first identifying the best phase shift  $\varphi_{r,0}$  of the azimuth angle in a 10 min instance, which is the initial point between the cumulative  $\varphi_m$  and  $\sum_i \omega_i \cdot \Delta t$ , using a few sequential data points. The instantaneous angle based on the rotor speed will be  $\varphi_{r,i} = \omega_i \cdot \Delta t + \varphi_{r,i-1}$ , for i > 1, and  $\varphi_{r,i} = \varphi_{r,0}$ , for i = 1. The final estimated azimuth is defined as  $\varphi_{e,i} = \varphi_{r,i} + K \cdot d$ , if  $d < d_{limit}$  and  $\gamma_{e,i} = \varphi_{r,i}$ , if  $d > d_{limit}$ . In which, d is the difference between the measured instantaneous angle and the estimation of the rotor speed  $d = \varphi_{m,i} - \varphi_{r,i}$ . The two manually tuned variables are the gain K and the distance limit  $d_{limit}$ . The first defines how reliable are the fluctuations from the measured azimuth. The latter correlates with the threshold of how many degrees the measured azimuth can realistically change within  $\Delta t$ . In this work, the parameters were tuned to K = 0.1 and  $d_{limit} = 30^\circ$ .

The validation was carried out in a good year (2019) by applying the method on 160 h of representative instances containing the Design Load Cases (DLC) 1.2, 3.1 and 4.1. The maximum instantaneous error  $/\varphi_m - \varphi_e/$  was below 5°.





# Appendix B: Statically indeterminate system of equations for a 4-point drivetrain considering a the gearbox mounting stiffness

Figure B1 shows the drivetrain schematic that allows one to derive the radial loads in the main bearings while considering the stiffness of the gearbox mounting. The vertical direction is chosen as it includes the most significant resultant loads (gravitational and aerodynamic), and the horizontal direction can be solved in the same manner.

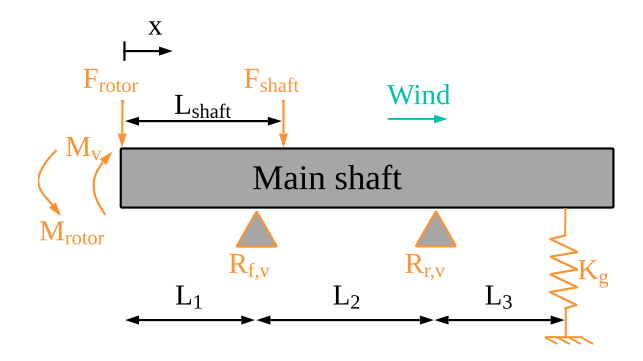


**Figure B1.** Drivetrain schematic used to represent the external loads applied and the supporting elements in the vertical direction.  $F_{rotor}$  and  $F_{shaft}$  are the rotor and shaft gravitational loads respectively,  $L_{shaft}$  the shaft center of mass distance,  $M_{rotor}$  the bending resultant from the rotor weight as the hub is not modeled, and  $M_v$  is the aerodynamical loading at the vertical direction. The main shaft is supported by the front  $R_{f,v}$  and rear  $R_{r,v}$  main bearings and by the gearbox through the equivalent spring  $K_g$ , which results in the force  $F_g$ .

The system of equations for the forces and bending moments is composed of:

$$\sum F = 0 = -F_{rotor} - F_{shaft} + R_{f,v} + R_{r,v} + F_g$$
(B1)

$$\sum M(x=0) = 0 = -M_v + M_{rotor} + R_{f,v}L_1 - F_{shaft}L_{shaft} + R_{r,v}(L_1 + L_2) + F_g(L_1 + L_2 + L_3)$$
(B2)

590 where the assumed sign conversion is upwards and anticlockwise as positive.

Since the system is statically indeterminate, there are two independent equations B1 and B2 and 3 unknowns reactions  $R_{f,v}$ ,  $R_{r,v}$  and  $F_g$ . To add a third equation, the main shaft is modeled as a flexible beam, with small deflections, linear material, and young modulus E and second area moment of inertia I constants along the length, as explained by Budynas and Nisbett (2020).

The following equations are used to describe the bending moment as a function of x and the beam deflection w along x through a double integration step.

$$EI\frac{d^2w}{dx^2} = M = -M_v + M_{rotor} + F_{rotor} \cdot x + F_{shaft} \cdot \langle x - L_{shaft} \rangle - R_{f,v} \cdot \langle x - L_1 \rangle - R_{r,v} \cdot \langle x - (L_1 + L_2) \rangle$$
 (B3)

$$EIw = -\frac{M_{v}}{2} \cdot x^{2} + \frac{M_{rotor}}{2} \cdot x^{2} + \frac{F_{rotor}}{6} \cdot x^{3} + \frac{F_{shaft}}{6} \cdot \langle x - L_{shaft} \rangle^{3} - \frac{R_{f,v}}{6} \cdot \langle x - L_{1} \rangle^{3} - \frac{R_{r,v}}{6} \cdot \langle x - (L_{1} + L_{2}) \rangle^{3} + C_{1} \cdot x + C_{2}$$
(B4)





600 where  $\langle \rangle$  is the Macaulay bracket or discontinuity function. To solve the constants  $C_1$  and  $C_2$ , two known boundary conditions (deflection at the main bearings) can be used as such:

$$w(x = L_1) = 0$$
 and  $w(x = L_1 + L_2) = 0$  (B5)

Finally, once the constants are calculated, the third independent equation can be derived by applying a third known boundary condition (deflection at the gearbox):

605 
$$w(x = L_1 + L_2 + L_3) = \frac{F_g}{K_g}$$
 (B6)

The resultant third independent equation is then:

$$EI\frac{F_g}{K_g} = -\frac{M_v}{2}(L_1 + L_2 + L_3)^2 + \frac{M_{rotor}}{2}(L_1 + L_2 + L_3)^2 + \frac{F_{rotor}}{6}(L_1 + L_2 + L_3)^3 + \frac{F_{shaft}}{6}(L_1 + L_2 + L_3 - L_{shaft})^3 - \frac{R_{f,v}}{6}(L_2 + L_3)^3 - \frac{R_{r,v}}{6}(L_3)^3 + C_1(L_1 + L_2 + L_3) + C_2$$
(B7)

The complete derivation are omitted for conciseness, consisting primarily of algebraic manipulation and variable substitution. Using the three independent equations B1, B2 and B7, and assuming quasi-static equilibrium at each time instant, one can calculate the 3 independent unknowns  $R_{f,v}$ ,  $R_{r,v}$  and  $F_{g}$ .

# Appendix C: Hyperparameters tuning of the data-driven virtual load sensors

The models described in Section 4.3 are tuned using a random search tuner (O'Malley et al., 2019) to improve the model performance. Table C1 shows the hyperparameters possible range and optimal value found for each virtual load sensor. Similarly to the methodology applied by Dimitrov and Göçmen (2022) and Gräfe et al. (2024), there are hyperparameters related to the data architecture, such as the number of lags  $n_{lags}$  in a NlaggedFNN and the window size in a LSTM, as well as hyperparameters related to the model architecture and training itself. The latter includes, for example, regularization features to improve the model generalization, such as the L2 regularizer and dropout. While, the model training was optimized in terms of batch size and learning rate. The range of parameters was similar to that used in Dimitrov and Göçmen (2022).





Table C1. Hyperparameter tuning, including the bound limits and optimum values for each model and feature possible combination.

		Optimal values							
Model	Hyperparameter	Parameter range	SCADA + Accelerometer	SCADA + Strain (one blade)	SCADA + Strain (all blade)	All			
Feedforward Neural Network (FNN)	Batch size	32:32:256	32	32	160	96	160		
	Learning rate	$10^{-4}:10^{-2}$	$2.5 \cdot 10^{-3}$	$5.8 \cdot 10^{-3}$	$7.2 \cdot 10^{-3}$	$3.0 \cdot 10^{-3}$	$3.5 \cdot 10^{-3}$		
	Hidden units	50:20:200	150	190	70	130	150		
	L2 regularizer	$10^{-6}:10^{-1}$	$2.0 \cdot 10^{-6}$	$3.6 \cdot 10^{-6}$	$1.2 \cdot 10^{-6}$	$11.3 \cdot 10^{-6}$	$2.8 \cdot 10^{-6}$		
	Second layer	0:1:2	1	1	1	0	0		
	Batch size	32:32:256	32	32	96	96	96		
	Learning rate	$10^{-4}:10^{-2}$	$0.8 \cdot 10^{-3}$	$0.8 \cdot 10^{-3}$	$1.8 \cdot 10^{-3}$	$2.8 \cdot 10^{-3}$	$1.7 \cdot 10^{-3}$		
lagged FNN	Hidden units	50:20:200	50	190	150	70	70		
(NlaggedFNN)	L2 regularizer	$10^{-6}:10^{-1}$	$1.4 \cdot 10^{-6}$	$1.2 \cdot 10^{-6}$	$4.6 \cdot 10^{-6}$	$1.6 \cdot 10^{-6}$	$5.2 \cdot 10^{-6}$		
	Second layer	0:1:3	0	1	0	0	0		
	$n_{lags}$	1:1:6	5	5	6	5	6		
Long Short-Term Memory NN (LSTM)	Batch size	32:32:256	128	64	64	64	64		
	Learning rate	$10^{-4}:10^{-2}$	$9.7 \cdot 10^{-3}$	$2.9 \cdot 10^{-3}$	$9.7 \cdot 10^{-3}$	$7.3 \cdot 10^{-3}$	$3.4 \cdot 10^{-3}$		
	Window size [s]	2,5,10,30	5	10	5	10	10		
	Dropout	0:0.1:0.5	0.1	0.2	0.2	0	0		

Author contributions. BF and AB participated in the conceptualization and design of the work together with DR and XZ. BF performed the
 measurements processing and conducted the data analysis. BF and ND performed the models training and deployment. BF and NS wrote the draft manuscript. AB, MS, ND and AK supported the results analysis. All reviewed and edited the manuscript.

Competing interests. Some authors are members of the editorial board of journal Wind Energy Science (WES).

Acknowledgements. This work is funded by the Department of Wind and Energy Systems at the Technical University of Denmark (DTU). The university also made the DTU research V52 turbine measurements available. The authors greatly appreciate the support. Special thanks to Steen Arne Sørensen and Søren Oemann Lind for their valuable support with the turbine database and for discussions on the instrumentation.





#### References

630

635

640

- ASTM D341-93: Viscosity-Temperature Charts for Liquid Petroleum Products, ASTM Standard ASTM D341-93 (Reapproved 1998), ASTM International, West Conshohocken, PA, USA, an American National Standard., 1998.
- ASTM E1049-85: Standard Practices for Cycle Counting in Fatigue Analysis, ASTM Standard ASTM E1049-85 (Reapproved 2017), ASTM International, West Conshohocken, PA, USA, 2017.
  - Bengio, Y., Simard, P., and Frasconi, P.: Learning long-term dependencies with gradient descent is difficult, IEEE Transactions on Neural Networks, 5, 157–166, https://doi.org/10.1109/72.279181, 1994.
  - Budynas, R. G. and Nisbett, J. K.: Shigley's Mechanical Engineering Design, McGraw-Hill Education, New York, NY, 11th edn., professor Emeritus, Kate Gleason College of Engineering, Rochester Institute of Technology; Associate Professor of Mechanical Engineering, Missouri University of Science and Technology, 2020.
  - D'Antuono, P., Weijtjens, W., and Devriendt, C.: On the Minimum Required Sampling Frequency for Reliable Fatigue Lifetime Estimation in Structural Health Monitoring. How Much is Enough?, in: European Workshop on Structural Health Monitoring, edited by Rizzo, P. and Milazzo, A., pp. 133–142, Springer International Publishing, Cham, ISBN 978-3-031-07254-3, 2023.
- de N Santos, F., Noppe, N., Weijtjens, W., and Devriendt, C.: Farm-wide interface fatigue loads estimation: A data-driven approach based on accelerometers, Wind Energy, 27, 321–340, https://doi.org/https://doi.org/10.1002/we.2888, 2024.
- Dimitrov, N. and Göçmen, T.: Virtual sensors for wind turbines with machine learning-based time series models, Wind Energy, 25, 1626–1645, https://doi.org/https://doi.org/10.1002/we.2762, 2022.
- DNVGL-RP-C203: Fatigue Design of Offshore Steel Structures Recommended Practice, Edition April 2016, DNVGL RP DNVGL-RP-C203:2016, DNV GL AS, Høvik, Norway, 2016.
- Faria, B. R. and Jafaripour, L. Z.: yaw-sweep-sg-cali: Strain-gauge yaw-sweep calibration for wind turbine towers, https://pypi.org/project/yaw-sweep-sg-cali/, version 3.2, 2023.
  - Faria, B. R., Sadeghi, N., Dimitrov, N., Kolios, A., and Abrahamsen, A. B.: Inclusion of low-frequency cycles on tower fatigue life-time assessment through relevant environmental and operational conditions, Journal of Physics: Conference Series, 2767, 042 021, https://doi.org/10.1088/1742-6596/2767/4/042021, 2024.
- 650 Faria, B. R., Dimitrov, N., Perez, V., Kolios, A., and Abrahamsen, A. B.: Virtual load sensors based on calibrated wind turbine strain sensors for damage accumulation estimation: a gap-filling technique, Journal of Physics: Conference Series, 3025, 012011, https://doi.org/10.1088/1742-6596/3025/1/012011, 2025.
  - Fingersh, L., Hand, M., and Laxson, A.: Wind Turbine Design Cost and Scaling Model, Technical Report NREL/TP-500-40566, National Renewable Energy Laboratory (NREL), Golden, CO, USA, https://doi.org/10.2172/897434, 2006.
- Gräfe, M., Pettas, V., Dimitrov, N., and Cheng, P. W.: Machine-learning-based virtual load sensors for mooring lines using simulated motion and lidar measurements, Wind Energy Science, 9, 2175–2193, https://doi.org/10.5194/wes-9-2175-2024, 2024.
  - Haastrup, M., Hansen, M. R., and Ebbesen, M. K.: Modeling of Wind Turbine Gearbox Mounting, Modeling, Identification and Control, 32, 141–149, https://doi.org/10.4173/mic.2011.4.2, 2011.
- Hart, E., Clarke, B., Nicholas, G., Kazemi Amiri, A., Stirling, J., Carroll, J., Dwyer-Joyce, R., McDonald, A., and Long, H.: A review of wind turbine main bearings: Design, operation, modelling, damage mechanisms and fault detection, Wind Energy Science, 5, 105–124, https://doi.org/10.5194/WES-5-105-2020, 2020.



680



- Hart, E., Raby, K., Keller, J., Sheng, S., Long, H., Carroll, J., Brasseur, J., and Tough, F.: Main Bearing Replacement and Damage A Field Data Study on 15 Gigawatts of Wind Energy Capacity, vol. NREL/TP-5000-86228, published by the US National Renewable Energy Laboratory (NREL) as Technical Report NREL/TP-5000-86228, July 2023., 2023.
- HIPERWIND D5.1: Component Life Models, Project Deliverable Deliverable D5.1, HIPERWIND Project HIghly advanced Probabilistic design and Enhanced Reliability methods for high-value, cost-efficient offshore WIND, Lyngby, Denmark, https://www.hiperwind.eu/deliverables-and-publications, 2023.
  - HIPERWIND D5.4: Development and implementation of probabilistic and uncertainty quantification methods for reliability sensitivity analysi, Project Deliverable Deliverable D5.4, HIPERWIND Project HIghly advanced Probabilistic design and Enhanced Reliability methods for high-value, cost-efficient offshore WIND, Lyngby, Denmark, https://www.hiperwind.eu/deliverables-and-publications, 2024.
  - Hoffmann, K.: An Introduction to Measurements Using Strain Gages, Hottinger Baldwin Messtechnik GmbH, Darmstadt, Germany, all rights reserved. © Hottinger Baldwin Messtechnik GmbH, 1989. Reproduction or distribution, in whole or in part, requires express written permission from the publisher., 1989.
- Hübler, C. and Rolfes, R.: Probabilistic temporal extrapolation of fatigue damage of offshore wind turbine substructures based on strain measurements, Wind Energy Science, 7, 1919–1940, https://doi.org/10.5194/wes-7-1919-2022, 2022.
  - IEA and NEA: Projected Costs of Generating Electricity: 2020 Edition, Tech. rep., International Energy Agency and OECD Nuclear Energy Agency, Paris, ISBN 978-92-64-55471-9, https://doi.org/10.1787/a6002f3b-en, 2020.
  - IEC 61400-1: Wind energy generation systems Part 1: Design requirements, Edition 4, IEC 61400-1:2019, International Electrotechnical Commission, Geneva, Switzerland, 2019.
    - IEC 61400-13: Wind energy generation systems Part 13: Measurement of mechanical loads, IEC 61400-13:2016, International Electrotechnical Commission, Geneva, Switzerland, 2016.
    - IEC-TS-61400-28: Wind energy generation systems Part 28: Through life management and life extension of wind power assets, IEC TS 61400-28:2020, International Electrotechnical Commission, Geneva, Switzerland, 2020.
- IRENA: Renewable Power Generation Costs in 2023, Tech. rep., International Renewable Energy Agency, Abu Dhabi, ISBN 978-92-9260-621-3, https://www.irena.org/Publications/2024/Sep/Renewable-Power-Generation-Costs-in-2023, 2024.
  - ISO-281: Rolling bearings Dynamic load ratings and rating life, ISO 281:2007, International Organization for Standardization, Geneva, Switzerland, 2007.
- Keller, J., Guo, Y., and Sethuraman, L.: Gearbox Reliability Collaborative: Investigation of Gearbox Motion and High-Speed690 Shaft Loads, Technical Report NREL/TP-5000-65321, National Renewable Energy Laboratory (NREL), Golden, CO, USA, https://doi.org/10.2172/1243302, 2016.
  - Kenworthy, J., Hart, E., Stirling, J., Stock, A., Keller, J., Guo, Y., Brasseur, J., and Evans, R.: Wind turbine main bearing rating lives as determined by IEC 61400-1 and ISO 281: A critical review and exploratory case study, Wind Energy, 27, 179–197, https://doi.org/10.1002/we.2883, 2024.
- Loraux, C. and Brühwiler, E.: The use of long term monitoring data for the extension of the service duration of existing wind turbine support structures, Journal of Physics: Conference Series, 753, 072 023, https://doi.org/10.1088/1742-6596/753/7/072023, 2016.
  - Mehlan, F. C., Keller, J., and Nejad, A. R.: Virtual sensing of wind turbine hub loads and drivetrain fatigue damage, Forschung im Ingenieurwesen, 87, 207–218, https://doi.org/10.1007/s10010-023-00627-0, 2023.
  - Miner, M. A.: Cumulative Damage in Fatigue, Journal of Applied Mechanics, 12, A159-A164, https://doi.org/10.1115/1.4009458, 1945.





- O'Malley, T., Bursztein, E., Long, J., Chollet, F., Jin, H., Invernizzi, L., et al.: KerasTuner, https://github.com/keras-team/keras-tuner, 2019. Pacheco, J., Pimenta, F., Guimarães, S., Castro, G., Álvaro Cunha, Matos, J. C., and Magalhães, F.: Experimental evaluation of fatigue in wind turbine blades with wake effects, Engineering Structures, 300, 117 140, https://doi.org/https://doi.org/10.1016/j.engstruct.2023.117140, 2024
- Papadopoulos, K., Morfiadakis, E., Philippidis, T. P., and Lekou, D. J.: Assessment of the strain gauge technique for measurement of wind turbine blade loads, Wind Energy, 3, 35–65, https://doi.org/https://doi.org/10.1002/1099-1824(200001/03)3:1<35::AID-WE30>3.0.CO;2-D, 2000.
  - Pedregosa, F., Varoquaux, G., Gramfort, A., Michel, V., Thirion, B., Grisel, O., Blondel, M., Prettenhofer, P., Weiss, R., Dubourg, V., VanderPlas, J., Passos, A., Cournapeau, D., Brucher, M., Perrot, M., Duchesnay, E., et al.: scikit-learn: Machine Learning in Python, https://scikit-learn.org/, journal of Machine Learning Research, 12:2825–2830, 2011.
- Pimenta, F., Ribeiro, D., Román, A., and Magalhães, F.: Predictive model for fatigue evaluation of floating wind turbines validated with experimental data, Renewable Energy, 223, 119 981, https://doi.org/https://doi.org/10.1016/j.renene.2024.119981, 2024.
  - Pulikollu, R., Haus, L., Mclaughlin, J., and Sheng, S.: Wind Turbine Main Bearing Reliability Analysis, Operations, and Maintenance Considerations: Electric Power Research Institute (EPRI), https://www.epri.com/research/products/00000003002029874, 2024.
- Rinker, J. M., Hansen, M. H., and Larsen, T. J.: Calibrating a wind turbine model using diverse datasets, Journal of Physics: Conference Series, 1037, 062 026, https://doi.org/10.1088/1742-6596/1037/6/062026, 2018.
  - Rumelhart, D. E., Hinton, G. E., and Williams, R. J.: Learning representations by back-propagating errors, Nature, 323, 533–536, https://doi.org/10.1038/323533a0, 1986.
  - Sadeghi, N., Noppe, N., Morato, P. G., Weijtjens, W., and Devriendt, C.: Uncertainty quantification of wind turbine fatigue lifetime predictions through binning, Journal of Physics: Conference Series, 2767, 032 024, https://doi.org/10.1088/1742-6596/2767/3/032024, 2024.
- 720 Santos, F. D. N., Noppe, N., Weijtjens, W., and Devriendt, C.: Data-driven farm-wide fatigue estimation on jacket-foundation OWTs for multiple SHM setups, WIND ENERGY SCIENCE, 7, 299–321, https://doi.org/10.5194/wes-7-299-2022, 2022.
  - Schaeffler TPI-176: Lubrication of Rolling Bearings, Technical Product Information TPI 176, Schaeffler Technologies AG & Co. KG, Herzogenaurach, Germany, principles; Lubrication methods; Lubricant selection and testing; Storage and handling., 2014.
  - Schillaci, M. A.: Estimating the population variance, standard deviation and coefficient of variation: sample size and accuracy, Statistics & Probability Letters, 188, 110 420, https://doi.org/10.1016/j.spl.2022.110420, 2022.
    - Scribd: V52–850 kW Wind Turbine Technical Specification (Vestas Document), https://www.scribd.com/document/524089466/v52, accessed: 2025-10-29, 2021.
    - SKF Group: SKF Product Select Single Bearing, https://productselect.skf.com/#/type-arrangement/single-bearing, accessed: 2025-10-27, 2025.
- 730 UNECE: Carbon Neutrality in the UNECE Region: Integrated Life-cycle Assessment of Electricity Sources, ECE Energy Series, United Nations, ISBN 978-92-1-001485-4, https://doi.org/10.18356/9789210014854, 2022.
  - Ziegler, L., Gonzalez, E., Rubert, T., Smolka, U., and Melero, J. J.: Lifetime extension of onshore wind turbines: A review covering Germany, Spain, Denmark, and the UK, Renewable and Sustainable Energy Reviews, 82, 1261–1271, https://doi.org/10.1016/j.rser.2017.09.100, 277 citations (Semantic Scholar/DOI) [2025-02-12], 2018.